Optimal design of an LCC-S WPT3 Z1 SAE J2954 compliant system, using NSGA-II with nested genetic algorithms for simultaneous local optimization

O. García-Izquierdo [a],[*], J.F. Sanz [a], J.L. Villa [a], G. Martin-Segura [b]

[a] *Instituto Universitario de Investigación Mixto CIRCE Universidad de Zaragoza-Fundación CIRCE, Zaragoza, Spain*
[b] *Wallbox Chargers, Barcelona, Spain*

ARTICLE INFO

ABSTRACT

Wireless Power Transfer (WPT) for electric vehicles is one of the most promising methods that, given its advantages, will drive the deployment of electric vehicles. This paper presents a mathematical optimization method applied to the complete design of an LCC-S WPT3 Z1 11 kW system that complies with the SAE J2954 standard (Wireless Power Transfer for Light-Duty Plug-in/Electric Vehicles and Alignment Methodology, 2020). A design method based on three phases is proposed, allowing the complete inductor system, including ferrites shielding and compensation circuit components, to function in any relative primary and secondary position. In Phase 1, a multi-objective NSGA-II algorithm is designed, utilizing three nested genetic algorithms. The goal is simultaneously searching for the local optimum between the primary and secondary systems in three positions. This is achieved by modeling the circuit's electrical and electromagnetic parameters with equations, enabling an iterative process with reduced computational time. The NSGA-II algorithm yields three scenarios: primary copper volume minimization, secondary copper volume minimization, and a compromise solution that optimizes the total volume. The result is then modeled in Phase 2 using a 3D finite element program that includes ferrite and optimal shielding, obtaining the values of inductances and mutual inductance in the three positions, as well as design data for manufacturing. This result is introduced in Phase 3 to optimize compensation circuit components using a second NSGA-II algorithm with three nested genetic algorithms. Again, three scenarios are obtained based on the desired system behavior and the optimal cost of the components. The result is validated through simulation with Matlab-Simulink and experimentally using a prototype constructed for this purpose.

1. Introduction

Wireless power transfer (WPT) presents an innovative approach to electric vehicle charging, being the only one that allows three scenarios: static, opportunistic, and dynamic. This versatility can help reduce battery size. In all cases, it must be able to work under different conditions of misalignment and height between primary and secondary, as well as battery voltage variation.

A range of resonant topologies has emerged. The simplest of these are called 'classical' resonant topologies, each defined by distinctive capacitor configurations: S–S, S–P, P–S, P–P, [1]. In topologies with a series connection on the primary side, a reduction in mutual impedance leads to an increase in primary current [2–5]. When the resonant capacitor is connected in parallel, it leads to a power reduction [2,4]. In both cases, precise control is required, and occasionally performance is reduced.

More complex topologies have been proposed to address these issues. Still, they come at a higher cost since they involve additional passive elements, such as the SP–S topology or the family of topologies using LCC on the primary side. The SP–S topology [6] allows for significant misalignments and height variations while maintaining power output without increasing the current in the inverter, which improves safety and simplifies control.

The LCC-S topology is prevalently used for delivering design power efficiently under significant variations in mutual inductance and battery voltage [3,7–12]. [12] has shown its superior efficiency over simpler configurations, such as S–S, justifying its selection for this study.

Additionally, the SAE J2954 standard [13] categorizes inductive systems into three power levels, namely WPT 1 (3.7 kW), WPT 2 (7.7 kW), and WPT 3 (11 kW), along with three transfer distances: Z1, Z2, and Z3. In this paper, a WPT3 Z1 LCC-S topology, compliant with the standard, is selected for optimization.

Various methodologies with different objectives have been proposed to optimize WPT systems. The work by [14] presents a classification and review of these methodologies. These optimization strategies can be broadly categorized into two main types: iterative methods and advanced algorithms.

Iterative methods, as proposed by [2,15–18], offer the advantage of consistently finding the optimal solution for the system. However, to limit computational time and address issues related to dimensionality, the number of variables included in the optimization is restricted. For example, in [2], the focus is on minimizing the number of turns of the inductors, and only four variables are optimized. Furthermore, the values of inductance and mutual inductance are obtained through equations. Other works, such as [15,16], extend this approach to systems with intermediate coils, utilizing finite element simulations (FEM) to consider materials like ferrites and aluminum in obtaining inductance and mutual inductance. [17] concentrates on optimizing efficiency by adjusting the number of turns, the inner coil size, and resonance capacitors. Lastly, [18] employs variable sweeps to obtain a set of Pareto diagrams with objective functions such as losses, power density, efficiency, and magnetic field dispersion. Additionally, they use 2D simulations to characterize the inductor system and estimate temperature, reducing computational cost by simplifying it to 2D simulations.

In contrast to iterative methods, advanced algorithms such as NSGA-II, which are based on genetic algorithms, have been introduced [14, 19–22]. In [19], an optimization based on NSGA-II is presented, incorporating an initial variable selection step through sensitivity analysis, reducing the problem's dimensionality and cutting the computational time in half compared to not performing sensitivity analysis. In [20], the inductor system is designed using FEM, with objective functions defined by the coupling coefficient (k) and magnetic flux magnitude. In [21] optimizes only the resonant capacitors in an LCC-LCC topology, as the coils are pre-determined. In [22], a comparison between NSGA-II and MOPSO for shielding optimization is carried out, with objective functions related to cost and mutual inductance.

Multi-objective methods based on PSO have also been proposed, as seen in [22–26]. In [23], ferrite optimization is performed to obtain maximum efficiency and power transfer while minimizing flux dispersion through asymmetric 2D simulations. [24] optimizes various classic topologies, considering wire cross-section, the number of turns, and the number of layers to achieve the most efficient system with minimal volt–amperes. [25] proposes a methodology for an S-CLC topology that allows obtaining compensation coils and capacitor values for a specific range of magnetic coupling and load. In [26], a methodology for an LCC-S system is presented, enabling the design of compensators for a specific operating range and loads, with the primary and secondary coils considered predefined.

Hybrid optimization methodologies, which combine different algorithms for enhanced effectiveness, have been developed [27–29].

In the literature reviewed for WPT system design, only [14] has used a hybrid optimization method for the calculation of an S–S WPT compliant with SAE J2954 [13]. It employs a multi-objective NSGA-II algorithm in combination with the secant method local algorithm. This method obtains optimal primary and secondary coils: the number of turns, wire cross-section, number of strands, inductance, mutual inductance, and calculates the resonance capacitors for both primary and secondary, although it does not consider ferrites or aluminum shielding.

Finally, [30] demonstrates an optimization method for the shape and arrangement of ferrites, improving the behavior against misalignment, but at the cost of greater complexity for its manufacture. This methodology has also given good results in the field of electrical machines, but with complex solutions at the manufacturing level, [31].

In all the papers reviewed, the optimization of the coils is performed exclusively in nominal position. Only two articles, [25,26], optimize compensators based on predefined coils for a range of coil positions through discretization of the coupling coefficient (k) and the equivalent circuit resistance (R_L). However, none of these articles consider the inductance variation when changing the positions of the coils and do not propose solutions by controlling the frequency and/or the output voltage.

From the conducted literature review, the following conclusions can be drawn:

- Advanced optimization methods reduce computational time.
- A priori, it is challenging to determine which algorithm is better for a specific problem, and no algorithm stands out from the rest [32]. However, hybrid algorithms have enhanced results in both classic and academic problems [29].
- Reducing variables is key to decreasing calculation time [19].
- None of the articles optimizes coils considering misalignment and airgap variation. The optimization is limited to the nominal position in all cases. Some subsequently evaluate the performance in other positions, sometimes only as expected.

The primary motivation of this work is to design an LCC-S WPT3 Z1 11 kW system that complies with the SAE J2954 standard [13]. This system should be cost-optimized and include all its components: inductive coils, ferrite, aluminum shielding, capacitors, and a filter coil for all defined working positions according to the standard. The standard also introduces constraints regarding system frequency and geometry to ensure interoperability. Additional constraints proposed by the designers are included in the development. These include achieving an efficiency higher than 95% and compliance with the circuit components' maximum current and voltage limits. The optimization process yields the following results:

- Inductors: the number of turns, wire cross-sections, and the number of strands are minimized to reduce cost.
- Shielding, minimizing its cost, consisting of:

    - Ferrite material: number, dimensions, and position.
    - Aluminum shielding: dimensions and position.

- The electrical circuit capacitors and filtering inductance values are optimized to minimize the solution's overall cost.

The optimization process ensures that the system can deliver the design power (P_D = 11 kW) for any secondary position relative to the primary in height and misalignment terms, as defined by the standard. This work develops a procedure consisting of three Phases to achieve this goal. Phase 1 involves designing a multi-objective genetic algorithm NSGA-II with three nested genetic algorithms. The NSGA-II algorithm, as in [14], calculates the optimal primary and secondary coils: the number of turns and wire cross-section. Two competing objective functions are defined, resulting in a Pareto optimal set and three decision scenarios: minimizing ground copper volume, onboard copper volume, or both simultaneously. The three nested genetic algorithms within NSGA-II are used to simultaneously obtain the optimal solution that works in three positions: nominal, centered with minimum height, and maximum misalignment with maximum height. If the system works well in these positions, it is expected to perform well in any other position. Mathematical equations presented in [14] model the inductances and resistances, allowing them to be included in the algorithms and minimizing the computation time. Once the optimal solution is selected according to the desired scenario, Phase 2 involves creating a 3D model using finite element analysis (FEA), which includes ferrite material and aluminum shielding. This model provides the values of inductances and resistances of the complete system in the three previously mentioned positions, along with all design parameters necessary for system manufacturing. In Phase 3, the result obtained in Phase 2 is introduced in the second NSGA-II algorithm, also with three nested genetic algorithms, to optimally calculate resonant capacitors and the filtering coil, as well as the frequency and the input and output voltages to give the design

power. This is done to operate correctly in the three positions defined above, considering a set of operating constraints. For this purpose, two objective functions are defined, generating a new Pareto optimal set. Additionally, three decision scenarios are considered: behavior leaning towards an S–S topology, behavior leaning towards a P–S topology, and behavior lying between both topologies. This makes it possible to determine the most suitable combination that performs as desired and minimizes costs.

The obtained results are validated in the various positions defined by the standard using Matlab-Simulink and experimental tests.

Therefore, the main contributions of this work are the following. It is the only one addressing the comprehensive design of the WPT system, ensuring proper operation in any position accepted by the standard. The method enables the inclusion of design restrictions on circuit components, thereby minimizing costs. The results include voltage values and frequencies at which the target power is obtained, facilitating the design of power electronics characteristics, with design restrictions also accounted for. This is one of the first WPT studies to combine two different methodologies in electromagnetic analysis: equations in the genetic algorithms, reducing computational costs, and FEM for shielding design, obtaining values very close to the real ones. This is the first work that proposes the joint treatment of the weighting variables KC_1 and KC_3 for the calculation of the compensators of the LCC-S topology to optimize its behavior. No other paper has been found to utilize NSGA-II with three nested genetic algorithms to design WPT systems comprehensively. Finally, the proposed method can be used to design any WPT by adapting the circuit equations and selecting the optimized parameters.

The paper is structured as follows: Section 2 explains the electrical circuit equations of the LCC-S topology. Section 3 defines the parameters set by SAE J2954 [13], the parameters to be optimized, and their limits. It also defines the parameters considered as variables to control. Section 4 explains the mathematical equations proposed for the electromagnetic modeling of resistances and inductances used in the NSGA-II algorithm. It also explains the equations for obtaining these values in the 3D finite element modeling. Section 5 explains the process followed in the optimization methodology, which is divided into three phases. Section 6 details the calculation process for Phases 1 and 3, explaining the NSGA-II algorithm for each and the three nested algorithms: GA1, GA2, and GA3. Finally, it presents the optimal solutions for each Phase. As the calculation process is the same and only the variables and objective functions change, they are presented simultaneously in the same section. Section 7 explains the modeling process corresponding to Phase 2, which includes ferrite and aluminum shielding, obtaining the solution for this phase. Section 8 validates the results obtained, firstly comparing the inductance values obtained by finite element modeling with the results of the manufactured coils. Secondly, it checks the system's operation, comparing the results obtained with equations with those obtained by modeling in Matlab-Simulink and those of the experimental test bench. Finally, Section 9 presents the main conclusions obtained.

In this paper, the subscript "p" refers to the primary, and the subscript "s" refers to the secondary. When referring to both simultaneously, "ps" is employed. For example, N_p refers to the number of turns in the primary coil, N_s to the number of turns in the secondary coil, and N_{ps} to the number of turns in both coils simultaneously.

2. Equivalent circuit of the LCC-S topology

The LCC-S topology (Fig. 1) is a combination of the classic S–S and P–S topologies in which the compensation in the primary is distributed between two capacitors, denoted C_1 connected in series, and C_3 connected in parallel. Assigning different weights to these capacitors makes the system's behavior more akin to the S–S or P–S topology in response to changes in position and battery voltage. To avoid short circuits, adding the auxiliary coil L_3 is necessary. Series

compensation is employed on the secondary side to ensure that the reflected impedance has no imaginary part, simplifying the calculation of the primary capacitors and the number of passive components.

The primary LCC topology is employed in compliance with SAE J2954 standard [13] and offers several advantages compared to other topologies, as described by [11,12,33]:

- It enhances efficiency compared to simpler topologies.
- It allows operation with more significant misalignment.
- It enables the reduction of inverter current and its variability, as opposed to topologies like S–S.

The system modeling incorporates the following simplifications:

- First harmonic approximation: The input voltage is modeled as sinusoidal.
- The battery is represented using an equivalent resistance R_L, assuming operation exclusively in continuous mode.

The primary power electronics consist of a full DC/AC bridge. At the same time, the secondary side features an uncontrolled AC/DC rectifier, along with a DC/DC voltage regulator, allowing adjustment of the secondary output voltage (V_s) to match the battery voltage.

The battery is modeled as an equivalent resistor R_L [34], using its voltage (V_{bat}) and the power objective (P_D). As a controllable secondary DC/DC converter is proposed, the battery is modeled using V_s instead of V_{bat}.

$$R_L = \frac{8}{\pi^2} \frac{V_s^2}{P_D} \tag{1}$$

The calculation process of capacitors C_1, C_3, and the auxiliary coil L_3 can be performed using the traditional method or the capacitor weighting method [11], which employs two weighting constants for the calculation of capacitors C_1 and C_3, denoted as KC_1 and KC_3, both greater than 1.

The traditional method selects capacitors C_1 and C_3, along with inductance L_3, to maintain the current in the primary coil I_{Lp} constant at a desired design value. This ensures that the current supplied by the source I_p and the current in the coil I_{Lp} remain constant, regardless of variations in coupling parameters (airgap, misalignment, battery voltage, etc.). This method represents a specific case of the weighting constants KC_1 and KC_3 within the capacitor weighting method.

The capacitor weighting method involves an iterative process to calculate KC_1 and KC_3, ensuring that the system complies with the desired design conditions. The calculation process is based on the fundamental equations of the circuit shown in Fig. 1, which is explained below.

The voltage V_{C3} at the capacitor C_3 is:

$$\overline{V_{C3}} = \overline{V_p} - jL_3w\overline{I_p} = \frac{\overline{I_{C3}}}{jC_3w} = \left(R_p + j\left(L_pw - \frac{1}{C_1w}\right)\right)\overline{I_{Lp}} - jMw\overline{I_s} \tag{2}$$

where V_p and I_p are the voltage and current at the output of the primary DC/AC bridge, R_p and L_p are the resistance and inductance of the primary coil, M is the mutual inductance between inductors, I_{Lp} and I_s are the currents through the primary and secondary coils respectively, and w is the angular frequency. The equation in the secondary of the circuit is as follows:

$$0 = \left((R_s + R_L) + j\left(L_sw - \frac{1}{C_2w}\right)\right)\overline{I_s} - jwM\overline{I_{Lp}} \tag{3}$$

R_s and L_s represent the secondary coil's resistance and inductance, respectively, and C_2 is the secondary resonant capacitor.

The current I_p at the output of the DC/AC bridge is:

$$\overline{I_p} = \overline{I_{C3}} + \overline{I_{Lp}} \tag{4}$$

Being I_{C3}:

$$\overline{I_{C3}} = jC_3w\overline{V_{C3}} = (\overline{V_p} - jL_3w\overline{I_p})jC_3w \tag{5}$$

(a) Electronic model

(b) Simplification model

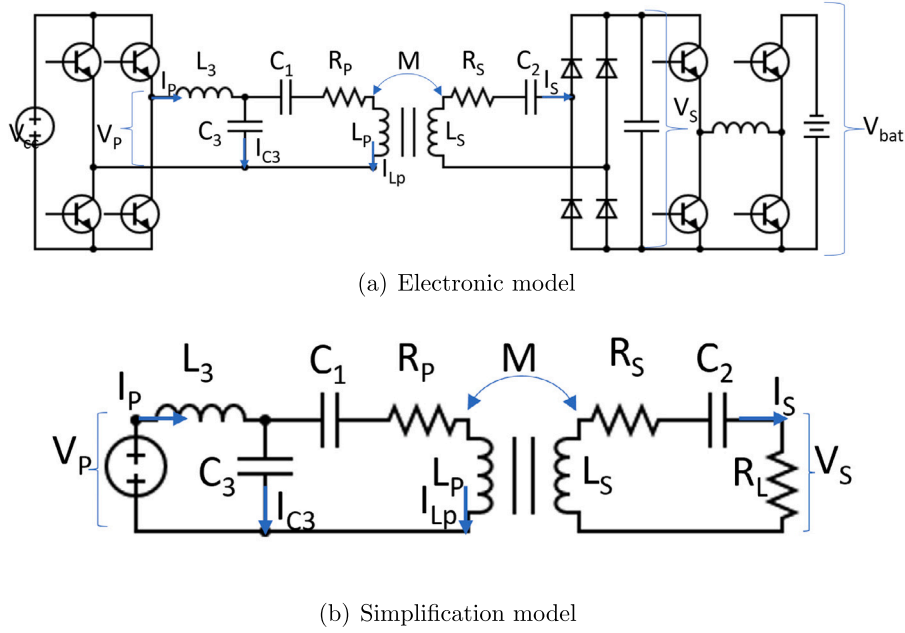Fig. 1. Simplification of the proposed electronic system.

The current in the secondary I_s, as a function of I_{Lp}, is given in (6):

$$\overline{I_s} = \frac{jwM\overline{I_{Lp}}}{R_s + R_L + j\left(L_s w - \frac{1}{C_2 w}\right)} \tag{6}$$

Considering that the secondary works in resonance, the value of C_2 is obtained from the value of the inductance L_s:

$$C_2 = \frac{1}{L_s w^2} \tag{7}$$

Substituting in (6):

$$\overline{I_s} = \frac{jwM}{R_s + R_L}\overline{I_{Lp}} \tag{8}$$

Substituting (8) in (2) leads to the following:

$$\overline{V_{C3}} = \overline{V_p} - jL_3 w\overline{I_p} = \left(R_p + j\left(L_p w - \frac{1}{C_1 w}\right)\right)\overline{I_{Lp}} + \frac{M^2 w^2}{R_s + R_L}$$
$$= (\overline{Z_p} + \overline{Z_r})\overline{I_{Lp}} = \overline{Z1I_{Lp}} \tag{9}$$

where Z_p is the primary impedance and Z_r is the secondary impedance reflected in the primary, which only has a real component when it is at resonance:

$$\overline{Z_r} = \frac{M^2 w^2}{R_s + R_L} \tag{10}$$

Next, a virtual primary capacitor C_1' is calculated to work in resonance with the coil L_p, mimicking an S–S topology, without considering L_3 or C_3:

$$C_1' = \frac{1}{L_p w^2} \tag{11}$$

To achieve P–S behavior of the topology, a capacitor C_1 larger than C_1' is selected by a factor $KC_1 > 1$ such that:

$$C_1 = KC_1 C_1' \tag{12}$$

Note that if $KC_1 = 1$ were chosen, the topology would be an S–S topology. Because $KC_1 > 1$, the coil's impedance exceeds that of the capacitor:

$$L_p w > \frac{1}{C_1 w^2} \tag{13}$$

Thus, the impedance Z_1, as observed by the source supplying the hypothetical S–S circuit, becomes inductive:

$$\overline{Z_1} = R_p + \frac{M^2 w^2}{R_s + R_L} + j\left(L_p w - \frac{1}{C_1 w}\right) = R_1 + jL_1 w \tag{14}$$

This impedance presents an inductive part L_1. Adding a new capacitor C_3' in parallel with Z_1 is necessary to compensate for it, thus obtaining the P–S behavior. This capacitor is calculated to cancel the imaginary part, obtaining a new impedance Z_2:

$$\overline{Z_2} = \overline{Z_1} // \frac{1}{jC_3' w} = \frac{R_p + \frac{w^2 M^2}{R_s + R_L} + j\left(L_p w - \frac{1}{C_1 w}\right)}{1 + j\left(R_p + \frac{w^2 M^2}{R_s + R_L} + j\left(L_p w - \frac{1}{C_1 w}\right)\right)C_3' w} \tag{15}$$

The virtual capacitor C_3' which cancels the imaginary part of Z_2 is:

$$C_3' = \frac{\left(L_p w - \frac{1}{C_1 w}\right)}{\left(R_p + \frac{w^2 M^2}{R_s + R_L} + \left(L_p w - \frac{1}{C_1 w}\right)^2\right)} \tag{16}$$

Adding this capacitor would render the total impedance seen from V_p purely resistive. However, by placing the capacitor in parallel with the source, it is necessary to add a protective auxiliary coil L_3 to limit current peaks. The total impedance Z_T seen by the source will be:

$$\overline{Z_T} = \overline{Z_2} + jL_3 w \tag{17}$$

As Z_2 is purely resistive, impedance Z_T exhibits inductive behavior. To compensate for it, it is necessary first to increase the value of the capacitor C_3' and then calculate the value of the inductance L_3. To achieve this, a factor $KC_3 > 1$ is defined, determining a capacitor C_3 larger than C_3':

$$C_3 = KC_3 C_3' \tag{18}$$

Eqs. (12), (13), (16), and (18) illustrate how capacitor C_3 is influenced by the value of KC_1:

$$C_3 = KC_3 C_3' = KC_3 \frac{\left(L_p w - \frac{1}{KC_1 C_1' w}\right)}{\left(R_p + \frac{w^2 M^2}{R_s + R_L} + \left(L_p w - \frac{1}{KC_1 C_1' w}\right)^2\right)} \tag{19}$$

When capacitor C_3 is added, the total impedance Z_T becomes capacitive. Therefore, the auxiliary coil L_3 must be calculated to render the impedance resistive, effectively eliminating the imaginary part of Z_T:

$$L_3 = \frac{C_3 w \left(\left(w R_p + \frac{w^2 M^2}{R_s + R_L} \right)^2 + \left(L_p w - \frac{1}{C_1 w} \right)^2 \right) - \left(L_p w - \frac{1}{C_1 w} \right)}{C_3^2 w^3 \left(\left(w R_p + \frac{w^2 M^2}{R_s + R_L} \right)^2 + \left(L_p w - \frac{1}{C_1 w} - \frac{1}{C_3 w} \right)^2 \right)} \quad (20)$$

This method enables adjustment of the WPT system's operation to meet the designer's requirements. Analyzing (19), it can be seen that if $KC_1 = 1$, capacitor $C_3 = 0$, meaning it is unnecessary, causing the system to behave as an S–S. If $KC_1 > 1$, it becomes necessary to add capacitor C_3, causing the system to behave like a P–S topology. If a very high value of KC_3 is chosen, the system tends to behave like an S–S topology again. The desired behavior between S–S and P–S is adjusted by the two variables KC_1 and KC_3. In general, $KC_1 \geq KC_3$ is assumed.

The power delivered to the secondary (P_s) is given by the secondary current I_s and the equivalent resistance R_L:

$$P_s = I_s^2 R_L = I_s^2 \frac{8}{\pi^2} \frac{V_s^2}{P_D} \quad (21)$$

Given that the controlled parameters are the voltages V_p and V_s, along with the frequency, it is essential to derive the power value as a function of these variables. Substituting I_s (8) it is obtained:

$$P_s = \left(\frac{jwM}{R_s + R_L} I_{Lp} \right)^2 \frac{8}{\pi^2} \frac{V_s^2}{P_D} \quad (22)$$

From (4) is obtained:

$$\overline{I_{Lp}} = \overline{I_p} - \overline{I_{C3}} = \frac{\overline{V_{C3}}}{\overline{Z_1}} \quad (23)$$

Substituting in (4), (5) in (23):

$$\overline{I_p} = \overline{I_{C3}} + \overline{I_{Lp}} = jC_3 w \overline{V_{C3}} + \frac{\overline{V_{C3}}}{\overline{Z_1}} = \frac{j\overline{Z_1}C_3 w + 1}{\overline{Z_1}} \overline{V_{C3}} \quad (24)$$

Solving for I_p in (2) can also be expressed as:

$$\overline{I_p} = \frac{\overline{V_p} - \overline{V_{C3}}}{j L_3 w} \quad (25)$$

From (24) and (25) V_{C3} is obtained as a function of V_p.

$$\overline{V_{C3}} = \frac{\overline{Z_1} \overline{V_p}}{j L_3 w (1 + j \overline{Z_1} C_3 w) + \overline{Z_1}} \quad (26)$$

Substituting in (23), I_{Lp} as a function of V_p is obtained:

$$\overline{I_{Lp}} = \frac{\overline{V_{C3}}}{\overline{Z_1}} = \frac{\overline{V_p}}{j L_3 w (1 + j \overline{Z_1} C_3 w) + \overline{Z_1}} \quad (27)$$

Finally, substituting the previous equation in (22), it is obtained the power delivered to the load (P_s) as a function of the controllable voltage of the primary (V_p) and the controllable voltage of the secondary (V_s):

$$P_s = \left(\frac{jwM}{R_s + R_L} \frac{\overline{V_p}}{j L_3 w (1 + j \overline{Z_1} C_3 w) + \overline{Z_1}} \right)^2 \frac{8}{\pi^2} \frac{V_s^2}{P_D} \quad (28)$$

As evident from (28), the power delivered to the load depends not only on the design power (P_D) but also on two distinct parameter sets:

- Constant parameters to optimize: formed by the electrical components of the circuit: L_p, L_s, M, R_p, R_s, C_1, C_2, C_3, L_3 with capacitors C_1 and C_3 related to each other by parameters KC_1 and KC_3.
- Variable parameters to control: those that can be controlled to adapt the operation to different height and misalignment situations: V_p, V_s, and f.

Table 1
Fixed parameters according to a WPT3 Z1 of SAE J2954 standard [13].

Parameter	Value
X-axis misalignment [cm]	10
Y-axis misalignment [cm]	7.5
Height variation Z [cm]	10–15
P_D design power [kW]	11

Table 2
External measurements corresponding to WPT Z1 of SAE J2954 standard [13].

Parameter [mm]	Value
a_p	650
b_p	500
a_s	380
b_s	380

Table 3
Maximum and minimum values of the parameters to be optimized.

Parameter	Minimum	Maximum
S_p [mm^2]	1	80
N_p	1	20
S_s [mm^2]	1	80
N_p	1	20
KC_1	1	10
KC_3	1	10

3. Design parameters

The system to be optimized is a WPT 3 Z1 LCC-S of 11 kW in compliance with SAE J2954 standard [13], considering square coils; therefore, some of the system variables are fixed by this standard (Table 1):

The optimization of the system will be performed considering three positions that define the nominal, maximum, and minimum values of the coil inductances L_p, L_s and the mutual inductance (M):

- Position 1: Centered and center height ($X = 0$ cm, $Y = 0$ cm; $Z = 12.5$ cm), corresponding to the nominal position, obtaining the nominal or design mutual inductance, L_p, L_s and M.
- Position 2: Centered and minimum height ($X = 0$ cm, $Y = 0$ cm; $Z = 10$ cm), obtaining L_{pmax}, L_{smax}, M_{max}.
- Position 3: Maximum misalignment and maximum height ($X = 7.5$ cm, $Y = 10$ cm; $Z = 15$ cm), obtaining L_{pmin}, L_{smin}, M_{min}.

The standard does not require compliance with specific dimensions for the coils, but it specifies particular dimensions for each case. Therefore, the external measurements corresponding to WPT Z1 coils are taken, as shown in Table 2.

Where "a" is the outer width and "b" is the outer length of each inductor.

In Section 2, the parameters of the WPT system have been classified between constants to be optimized and variables to be controlled.

Among the constant parameters, the values of compensators C_1, C_2, C_3, L_3, can be calculated using (11), (16), (18), (19) and (20), utilizing the values of KC_1 and KC_3 to adjust the behavior of the topology. Furthermore, the values of L_p, L_s, M, R_p and R_s are also mathematically modelable through (29) to (33), which are explained in Section 4 and are determined by the cross-sectional area (S) of the conductors and the number of turns (N).

Table 3 shows the maximum and minimum values considered for the optimization of the constant parameters.

Regarding the variable parameters to be controlled to obtain the P_D power in the secondary, maximum and minimum values are also defined in Table 4.

V_p and V_s are delimited by the power electronic converters to be used, and the Standard defines the range of variation of f. Finally,

Table 4
Maximum and minimum values of the variable parameters to be controlled.

Parameter	Minimum	Maximum
V_p [V]	600	800
V_s [V]	300	800
f [kHz]	79	90

a series of restrictions in the design will be considered regarding the current and voltages imposed on the different elements of the circuit, which are explained in Section 6. Likewise, the standard sets a minimum efficiency of 85% in the centered position and 80% in any working position; in this paper, the efficiency of the WPT system, discounting the electronics, is set at 99%.

4. Electromagnetic model

For the solution of the electrical circuit, it is necessary to obtain the values L_p, L_s, M, R_p, and R_s of the circuit (Fig. 1). To do this, electromagnetic modeling is necessary, which can be carried out in the following ways:

- Modeling using mathematical equations [2,35]: In this type of modeling, simplification is performed by considering only the ideal inductor, i.e., the ferrite and shielding are not taken into account. The main advantage is the calculation time [14].
- FEM modeling [36,37]: In this type of electromagnetic modeling, finite element analysis programs are used, and it involves solving Maxwell's equations. This type of modeling allows for the inclusion of ferrite and aluminum shielding, improving result accuracy.

Both methods are used in this work. In Phase 1, the system is optimized using genetic algorithms to model the inductors (L_p, L_s, M, R_p, and R_s) using equations without considering ferrite and aluminum. In Phase 2, the inductors are modeled, including ferrite and aluminum, using FEM modeling, obtaining L_p, L_s, and M in the three positions previously indicated. In Phase 3, genetic algorithms are also used for the complete system, with the difference from Phase 1 being that the values of inductances have already been definitively calculated in Phase 2. However, the values of resistances (R_p and R_s) are recalculated in the same way as in Phase 1 since, unlike inductances, they depend on the frequency.

4.1. Mathematical electromagnetic modeling

4.1.1. Mathematical modeling of inductances L_p and L_s, Phase 1
The value of the inductance of each coil is obtained from [14,35]:

$$L = 2N_i^2(L_a + L_b - (M_a + M_b))\quad(29)$$

where L_a and L_b are obtained from (30):

$$L_c = \frac{\mu_0 c}{2\pi}\left(\log(\sqrt{(c^2 + AMSD_L^2)} + c) - \log GMD_L \right.$$
$$\left. - \sqrt{1 + \left(\frac{AMSD_L}{c}\right)^2} + \frac{AMD_L}{c}\right)\quad(30)$$

In the equation provided, c represents the average length of either the a or b side of the coil, μ_0 denotes the magnetic permeability of a vacuum, and $AMSD_L$, GMD_L, and AMD_L stand for the compound mean distances associated with the partial self-inductance of the sides of the single-turn coil. The methodology for calculating these distances is detailed in [35]. The mutual inductance M_a, between the parallel turns of side a at an average mutual distance b, and the mutual

inductance M_b between the parallel turns of side b at an average mutual distance a, can be expressed as follows:

$$M_c = \frac{\mu_0 c}{2\pi}\left(\log(\sqrt{(c^2 + AMSD_{\bar{c}}^2)} + c) - \log GMD_{\bar{c}} \right.$$
$$\left. - \sqrt{1 + \left(\frac{AMSD_{\bar{c}}}{c}\right)^2} + \frac{AMD_{\bar{c}}}{c}\right)\quad(31)$$

where c is the average length of the coil's a or b side and $\bar{c}$ is the average length of the coil's b or a side. When $c = a$, then $\bar{c} = b$, and vice versa.

Experimental validation of the above equations can be found in [14].

4.1.2. Mathematical modeling of the mutual inductance M, Phase 1
The mathematical modeling of mutual inductance is performed by Eq. (32), which is an improved evolution of the Neumann's expression [1,14,38]:

$$M = \sum_{i=1}^{N1}\sum_{j=1}^{N2} M_{ij} = \sum_{i=1}^{N1}\sum_{j=1}^{N2}\frac{\mu_0}{4\pi}\iint\frac{dl_i dl_j}{r_{i,j}}\quad(32)$$

M_{ij} represents the mutual inductance between the ith turn of the primary and the jth turn of the secondary and r signifies the distance between corresponding current elements.

The value of the mutual inductance depends on the distance between the turns of the primary and secondary coils, so it varies with the relative position of the coils. Consequently, the calculation is conducted for the three positions mentioned in Section 3, obtaining M, M_{max}, and M_{min}.

4.1.3. Mathematical modeling of coil resistances, Phase 1 and Phase 3
The coil resistance values R_p and R_s are calculated considering Skin (R_{skin}) and Proximity (R_{prox}) effects using the next equations according to [14,39]:

$$R_i = R_{skin} + R_{prox} =$$
$$\frac{ber_0(\frac{\xi}{\sqrt{2}})beri_0'(\frac{\xi}{\sqrt{2}}) - beri_0(\frac{\xi}{\sqrt{2}})ber_0'(\frac{\xi}{\sqrt{2}})}{ber_0'(\frac{\xi}{\sqrt{2}})^2 beri_0'(\frac{\xi}{\sqrt{2}})^2}R_{dc}$$
$$- \frac{2\sqrt{2}\pi\varphi}{\delta}\frac{H^2}{I^2}\frac{ber_2(\frac{\xi}{\sqrt{2}})ber_0'(\frac{\xi}{\sqrt{2}}) + beri_2(\frac{\xi}{\sqrt{2}})bei_0'(\frac{\xi}{\sqrt{2}})}{ber^2(\frac{\xi}{\sqrt{2}})beri^2(\frac{\xi}{\sqrt{2}})}\quad(33)$$

where R_{skin} is expressed as the direct current resistance (R_{dc}) and a set of Bessel functions that account for the frequency-dependent penetration depth (ξ). R_{prox} is expressed as a function of the magnetic field intensity (H) and another set of Bessel functions representing the frequency dependence. To mitigate both skin effect (P_{skin}) and proximity (P_{prox}) losses attributed to the operating frequency, it is imperative to utilize Litz wire, as suggested by previous studies [18, 36,39], with an optimized strand diameter of 0.1 mm, as found to be the most efficient diameter within the system's frequency range [38]. Furthermore, the packing factor must be considered in determining the total coil cross-sectional area; in this instance, a factor of 0.5 has been considered [40].

4.2. Electromagnetic modeling using finite elements, Phase 2

In Phase 2, the coils obtained in Phase 1 are modeled using finite element analysis, incorporating ferrite and aluminum shielding. The modeling is performed to minimize any significant variation in the previously optimized values of L_p, L_s, and M from Phase 1 while reducing costs associated with ferrite usage. Furthermore, the distance between the coils affects the value of mutual inductance and the self-inductances L_p and L_s. This effect cannot be calculated using (29) but can be obtained through finite element analysis (FEM) simulations.
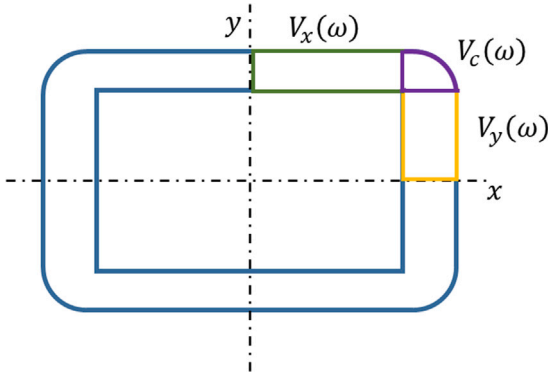
Fig. 2. Symmetry of the coil.

Consequently, in Phase 2, the values of inductances L_p, L_s, and M are calculated at the three Positions defined in Section 3.

The calculation described below is based on the methodology outlined in [36,37], in which the inductor system is defined with a homogeneous current density (J).

$$J = \frac{I}{S} \tag{34}$$

I is the current through the coil, and S is the equivalent inductor section.

The calculation of the induced voltage in the coils (V) is obtained as a function of the electric field in the coil:

$$V(w) = \int E(w)dl = \frac{-1}{S} \int E(w)\bar{l} \, dVol \tag{35}$$

Given E as the electric field, l as the vector defining the coil's direction, and $dVol$ as the derivative concerning the inductor's volume. Expanding this equation for the specific case under consideration (Fig. 2), it is observed that the system exhibits symmetry, enabling it to be divided into four equal parts, with each part consisting of three sectors. Applying the above equation to each of these sectors and multiplying by four yields [37]:

$$V(w) = \frac{-4}{S}(V_x(w) + V_c(w) + V_y(w)) = \frac{-4}{S} \left(\int E_x(w)\bar{x} \, dVol \right.$$
$$+ \int \left(-E_x(w)\frac{\bar{y}}{r} + E_y(w)\frac{\bar{x}}{r} \right) dVol +$$
$$\left. \int E_y(w)\bar{y} \, dVol \right) \tag{36}$$

Once the voltage is obtained, the inductance can be defined as the imaginary part of the ratio of the voltage to the current multiplied by the angular frequency [36,37], as follows:

$$L(w) = \frac{Imag(V(w))}{Iw} \tag{37}$$

Finally, the mutual inductance is defined as the ratio of the imaginary part of the inductor voltage, divided by the current in the other inductor multiplied by the angular frequency [36,37]:

$$M_{ps}(w) = M_{sp}(w) = \frac{Imag(V_p(w))}{I_s w} = \frac{Imag(V_s(w))}{I_p w} \tag{38}$$

5. Optimization methodology

The optimization methodology aims to dimension a complete 11 kW WPT 3 Z1 LCC-S system, including coils, ferrite, shielding, capacitors C_1, C_2, C_3, and filtering coil L_3, to minimize system costs while meeting standard requirements and designer-imposed restrictions. The developed process is divided into three phases:

- PHASE 1: Optimization of the simplified optimal system, without ferrite or aluminum. This phase determines parameters for the inductors, including the number of turns (N_{ps}), cross-sectional area (S_{ps}), and their inductances.
- PHASE 2: In this phase, the coils obtained in Phase 1 are modeled using finite element analysis (FEM), incorporating ferrite and aluminum shielding. The goal is to obtain inductance values in three positions, ensuring minimal deviation from the optimized values obtained in Phase 1 while minimizing the amount of ferrite used to control costs.
- PHASE 3: Optimization of the compensation components for the circuit: C_1, C_2, C_3, and L_3, along with the values of V_p, V_s, and f that allow operation in all positions. This phase ensures that the system operates efficiently across all positions defined in Phase 2 while meeting standard requirements and constraints imposed by designers.

For Phases 1 and 3, individual NSGA-II [41] genetic algorithms have been developed, each of which internally incorporates three genetic algorithms: GA1, GA2, and GA3. Phase 2 is conducted using the finite element analysis program.

In Phases 1 and 3, two competing objective functions are defined for each to be solved subject to a set of constraints. Hence, a multi-objective genetic algorithm (MOEA) is required to identify the optimal solutions that constitute the Pareto Front. The inclusion of elitism in these algorithms enhances their performance. Among the most widely utilized algorithms are NSGA-II by Pétrowski and Ben Hamida (2017), as well as SPEA, SPEA2, PAES, MOMGA, and MOMGA-II.

The NSGA-II algorithm, as presented in [14], is highly cited and widely used. It has been successfully applied across various engineering disciplines, including the design of complex electrical systems. The paper [14] offers a detailed example of NSGA-II's application. This example demonstrates the integration of NSGA-II with a secant-based local search algorithm for coil calculations in an S–S WPT system.

A multi-objective algorithm is characterized by having two or more conflicting objectives that must be simultaneously minimized or maximized while adhering to specific constraints.

In this category of problems, finding a perfect solution that optimizes all the objective functions is unattainable. However, it is possible to identify a set of non-dominant solutions, known as the Pareto Optimal Set, from which a solution relevant to the chosen scenario can be selected. Below, a summarized explanation of the optimization process for each phase is provided, along with the workflow and detailed equations presented in Section 6.

PHASE 1: Optimization of the simplified optimal system.

The optimal design of primary and secondary coils, excluding ferrite and shielding, is achieved by employing the NSGA-II algorithm, which integrates three nested genetic algorithms (GA1, GA2, GA3). This approach allows us to refine the coil design to meet specific criteria and objectives.

The design is engineered to function correctly in the three positions: Position 1, yielding M; Position 2, obtaining M_{max}; and Position 3, achieving M_{min}.

Using the initial random vectors generated by the NSGA-II algorithm and mathematical circuit parameter modeling, genetic algorithm GA1 calculates compensators (C_1, C_2, C_3 and L_3) based on preliminary values of KC_1 and KC_3. These compensators enable the system to achieve the desired power level P_D in Position 1 as well as the values of V_p, V_s, and f necessary for this purpose.

The result is simultaneously forwarded to genetic algorithms GA2 and GA3, which compute the values of V_p, V_s, and f to achieve power P_D in Positions 2 and 3, respectively.

If a solution exists for all three positions, it undergoes evaluation using the objective functions of the NSGA-II. This iterative process generates an optimal Pareto front. The objective of this optimization method is to minimize the use of copper in the system and to achieve this goal, three decision scenarios are considered [14]:

- Scenario 1: Minimization of primary coil cost (most suitable for shore coil manufacturers).
- Scenario 2: Minimizing secondary coil cost (most ideal for on-board coil manufacturers).
- Scenario 3: Balanced cost minimization (a compromise solution).

The selection of the most appropriate scenario depends on the designer's requirements. In this study, Scenario 3 was chosen as a compromise solution between the other two scenarios. Within this scenario, the solution with the highest mutual inductance (M) value was selected to reduce the current in the primary coil (I_{Lp}), consequently lowering the value of C_1. This selected solution, denoted as $S1$ (39), provides the number of turns (N_{ps}), cross-sectional area (S_{ps}), self-inductances (L_{ps}), and mutual inductances in three positions (M, M_{max}, and M_{min}) for each coil. Although the remaining circuit parameters are obtained, they are omitted in the solution $S1$ as they will be recalculated subsequently.

$$S1(N_{ps}, S_{ps}, L_{ps}, M, M_{max}, M_{min}) \tag{39}$$

PHASE 2: FEM-based system design, including shielding. The result ($S1$) is modeled using the FEM method by incorporating ferrites and an aluminum shield. The design objective is to achieve a complete system that closely maintains the values of self-inductances (L_{ps}) and mutual inductances (M, M_{max} and M_{min}), in the three positions to match the values of $S1$ closely. To accomplish this, the size of the aluminum sheet and the distances between the different components specified by the Standard are taken as starting points, along with the obtained values of S_{ps}. The number of primary and secondary turns (N_{ps}) is adjusted based on the value previously calculated in Phase 1, and adjustments are made to the surface area occupied by ferrites and the distance between ferrites and coils, as needed. The coils section S_{ps} is also modified if necessary.

The obtained result $S2$ (40) provides the complete geometry of the inductors, ferrites, and aluminum sheet and the values of mutual inductances and self-inductances in the three positions. In addition, from the graphical design of the 3D model, the necessary details for the construction of the system are also obtained.

$$S2(N_{ps}, S_{ps}, L_{ps}, L_{psmax}, L_{psmin}, M, M_{max}, M_{min}) \tag{40}$$

As explained earlier, the variation in self-inductances with position (L_{ps}, L_{psmin}, L_{psmax}) cannot be calculated through equations; however, it can be determined using finite element analysis. Thus, these values are obtained in Phase 2, not Phase 1.

PHASE 3: Optimization of the complete optimal system. NSGA-II is employed alongside three nested genetic algorithms in this phase, akin to Phase 1. The objective here is to optimize the circuit compensators C_1, C_2, C_3, and L_3 while concurrently determining the values of V_p, V_s, and f necessary for operation in the three positions.

Beginning with the outcome $S2$ from Phase 2, the NSGA-II algorithm generates a set of vectors with initial random values for KC_1 and KC_3, which are then utilized to derive the values of the compensator elements within the circuit. These values undergo initial evaluation in GA1, where the corresponding V_p, V_s, and f required to attain the target power P_D in the central position are calculated, if feasible. Should a solution be achieved for the central position, the compensator values are concurrently transmitted to the GA2 and GA3 algorithms. The values of V_p, V_s, and f are calculated to obtain the target power at the two remaining positions if there is a solution.

The outcomes of the three algorithms are returned to NSGA-II, where two objective functions produce a new Pareto Optimal Set, providing optimal results for KC_1 and KC_3. This results in three scenarios:

- Scenario 1: When KC_1 approaches 1, the system tends toward S–S behavior; conversely, an increase in KC_1 tends toward P–S behavior.

Table 5
Number of individuals in the population and maximum number of generations of the genetic algorithms ($Nmax_{GA}$).

	NSGA-II	GA 1	GA 2	GA 3
Population	500	400	100	100
Generation ($Nmax_{GA}$)	100	80	50	50

- Scenario 2: When KC_3 approaches 1, the system leans toward P–S behavior; however, an increase in KC_3 tends toward S–S behavior.
- Scenario 3: Represents intermediate behavior.

Since the objective is to leverage the advantages of the LCC-S topology over S–S and P–S, the desired solution lies within Scenario 3. This scenario, while meeting all constraints, delivers superior performance in current and voltage across passive elements while minimizing costs. This solution is not immediate and must be carefully selected to obtain the final optimal result $S3$.

$$S3(S2, KC_1, KC_3, C_1, C_2, C_3, L_3) \tag{41}$$

Phases 1 and 3 share a nearly identical structure and calculation process. As mentioned, each phase employs a multi-objective genetic algorithm, NSGA-II, and three internal genetic algorithms: GA1, GA2, and GA3. For this reason, both phases are simultaneously discussed in Section 6, and their workflow is illustrated in Figs. 3 and 4.

The objective functions and constraints considered of NSGA-II are elaborated in Step 5 of Section 6. The objective function and constraints of GA1 are detailed in Step 2.2, while those of GA2 and GA3 are presented in Step 2.3 and Step 2.4, respectively.

6. Optimization workflow for Phase 1 and Phase 3

Fig. 3 shows the computational procedure utilized in Phases 1 and 3, comprising 6 Steps:

- Step 1: Random initialization of the population.
- Step 2: Mathematical modeling of the system and calculation of NSGA-II objective functions.
- Step 3: Evaluation of solutions using the Non-dominance test and Crowding distance.
- Step 4: Tournament selection.
- Step 5: Obtaining the offspring using crossover and mutation operators.
- Step 6: Obtaining the final Pareto set and solution selections.

The process concludes once it reaches the predefined maximum number of generations.

Table 5 shows the values of populations maximum number of generations used ($Nmax_{GA}$) in the genetic algorithm described in the paper.

6.1. Step 1: Random initialization of the population

This step involves the random generation of $iMax$ vectors of decision variable vectors, denoted as $x_i \in X$. Each vector represents an individual within the initial population.

In Phase 1, the optimization focuses on the coils. Therefore, the initial random values are associated with the design of both coils, specifically N_{ps} and S_{ps}. Additionally, to solve the circuit, it is necessary to calculate the values of the capacitors. Thus, random values of KC_1 and KC_3 are generated within the specified maximum and minimum limits, as indicated in Table 3.

In Phase 3, the starting point is the well-designed coils from Phase 2, denoted as $S2$ (40), and only the capacitors and L_3 are optimized using KC_1 and KC_3, so these are the random values used.
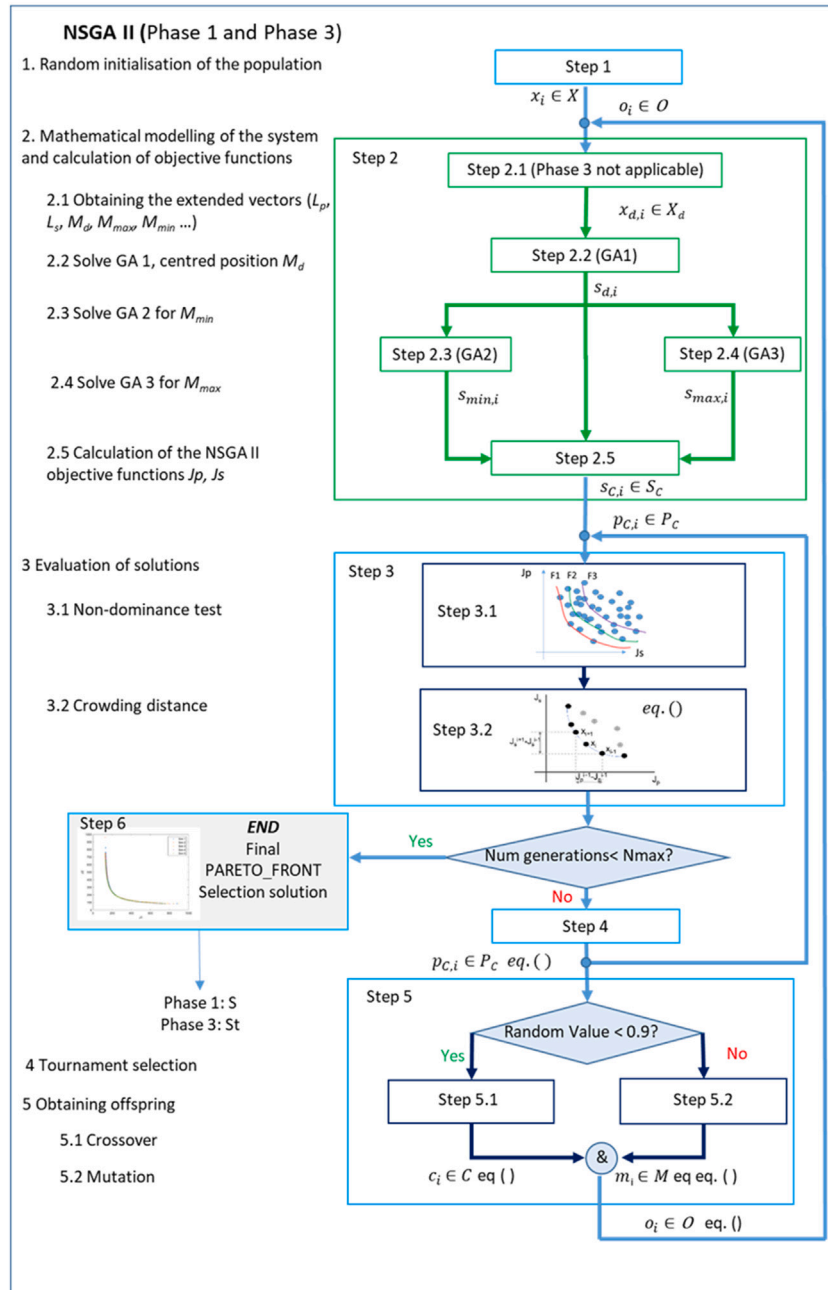
Fig. 3. Optimization workflow for Phases 1 and 3.

Finally, the counter variable 'i' is initialized at the beginning of both phases for tracking purposes.

$$Phase\ 1:\ Random\ values:\ N_{p,i}, S_{p,i}, N_{s,i}, S_{s,i}, KC_{1,i}, KC_{3,i}$$

$$Initial\ population:\ x_i\left(N_{p,i}, S_{p,i}, N_{s,i}, S_{s,i}, KC_{1,i}, KC_{3,i}\right) =$$

$$x_i\left(N_{ps,i}, S_{ps,i}, KC_{13,i}\right); x_i \in X\ ;\ i = 1\ldots iMax \quad (42)$$

$$Phase\ 3:\ Random\ values:\ KC_{1,i}, KC_{3,i}$$

$$Initial\ population:\ x_i\left(S2, KC_{1,i}, KC_{3,i}\right) = x_i\left(S2, KC_{13,i}\right); x_i \in X;$$

$$i = 1\ldots iMax \quad (43)$$

where KC_{13} refers to KC_1 and KC_3 together.

6.2. Step 2: Mathematical modeling of the system and calculation of NSGA-II objective functions

In Step 2 the genetic algorithms GA1, GA2, and GA3 are executed, comprising five internal steps:

- Step 2.1: Computation of the inductances L_{ps}, M, M_{max}, and M_{min}.
- Step 2.2: Design the optimal system at Position 1 using Genetic Algorithm GA1.
- Step 2.3: Validation of the solution obtained in Step 2.2 for Position 2 using GA2.
- Step 2.4: Validation of the solution obtained in Step 2.2 for Position 3 using GA3.
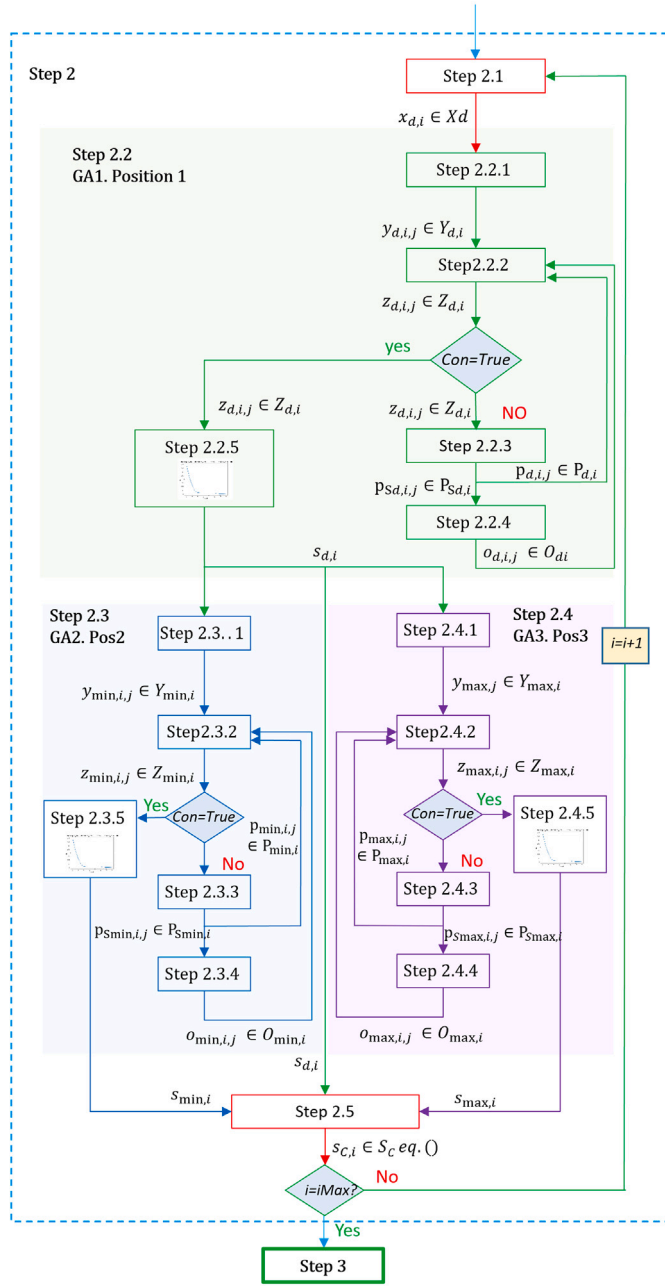- Step 2.5 Computation of NSGA-II Objective Functions

Fig. 4. Detailed workflow of Step 2.

In Phase 3, Step 2.1 is unnecessary because the values of the inductances L_{ps} and M in the three positions are already defined in $S2$, obtained as a result of Phase 2.

Fig. 4 shows the detailed workflow of Step 2.

6.2.1. Step 2.1: Calculation of the inductances L_{ps} and M, M_{max}, M_{min}

In Phase 1, the inductance values of the coils and mutual inductances are computed for each element x_i from Step 1, resulting in the updated elements $x_{d,i}$ (44).

However, in Phase 3, such calculation is not necessary since this data is available and fixed as a result of Phase 2. To maintain workflow clarity, the x_i values from Phase 3 are renamed $x_{d,i}$ (45) with no alterations to their values.

$$Phase\ 1: \ x_{d,i}\left(N_{ps,i}, S_{ps,i}, KC_{13,i}, L_{ps,i}, M_i, M_{max,i}, M_{min,i}\right) =$$
$$x_{d,i}\left(x_i, L_{ps,i}, M_i, M_{max,i}, M_{min,i}\right) \in X_d \tag{44}$$

$$Phase\ 3: \ Not\ applicable: x_i = x_{d,i} \in X_d \tag{45}$$

The inductances in (44) are calculated using (29) and (32).

6.2.2. Step 2.2: Design of the optimal system in Position 1 using Genetic Algorithm 1 (GA1)

In this step, a Genetic Algorithm is applied to each $x_{d,i}$ at Position 1, where the mutual inductance is given by M_i, to obtain a solution $s_{d,i}$ with values for C_1, C_2, C_3, and L_3 that achieve the power closest to the target power P_D. This process remains consistent in both Phases 1 and 3.

Step 2.2.1 Random initialization of GA1. To calculate the capacitors in the electrical circuit (Fig. 1), it is necessary to solve the equations in Section 2. This requires defining the values of the input voltage V_p, the output voltage V_s, and the frequency f. These values are randomly selected and assigned to each individual ($x_{d,i} \in X_d$) within specific limits, as outlined in Table 4.

In both Phases, $jMax$ random values of f_{ij}, $V_{P,ij}$ and $V_{S,ij}$ are assigned to each individual $x_{d,i}$ resulting in:

$$y_{d,ij}\left(x_{d,i}, f_{ij}, V_{p,ij}, V_{s,ij}\right) \in Y_{d,i}; i = 1...iMax; j = 1...jMax. \tag{46}$$

Here, $Y_{d,i}$ represents the set of parents for evaluation in the next step.

Step 2.2.2 Calculation of circuit parameters and objective function. In this step, during the first iteration, the Parents $y_{d,ij} \in Y_{d,i}$ obtained from 2.2.1 (46) are evaluated. During the second iteration and until the last one, the children $o_{d,ij} \in O_{d,i}$ from Step 2.2.4 (56) are evaluated, renaming the children in this case:

$$Y_{d,ij+1} = O_{d,ij} \tag{47}$$

For each $y_{d,ij}$, the process begins with the calculation of coil resistance values R_p and R_s based on (33). Then the circuit equations of Section 2 are solved with $KC_{13,ij}$ to obtain the values of the capacitors C_1, C_2, C_3, and the coil L_3. Finally, the common objective function $J_{PD,ij}$ given from the following equation is calculated, being the same for both Phases 1 and 3:

$$J_{PD,ij} = abs\left(P_{PD} - P_{S,ij}\right) +$$
$$K^2(\Delta VC_{123,ij} + \Delta VL_{ps3,ij} + \Delta I_{p,ij} + \Delta I_{Lp,ij} + \Delta I_{s,ij} + \Delta Arg(I_{p,ij})) \tag{48}$$

where $P_{S,ij}$ represents the power of each $y_{d,ij}$ calculated using (28).

This equation evaluates the offspring whose power $P_{S,ij}$ closely matches the target power P_{PD}. In an ideal scenario where $P_{S,ij} = P_{PD}$, the value of the objective function is zero: $J_{PD,ij} = 0$.

During the evaluation of the objective function, there may be cases where the currents or voltages of the system components are excessively high. To penalize these situations, the following parameters are included in Eq. (48): ΔVC_{123}, to take into account the voltages on capacitors VC_1, VC_2 and VC_3; ΔVL_{ps3}, to take into account the voltages at inductances VL_p, VL_s and VL_3; ΔI_p, ΔI_s, and ΔI_{Lp}, to take into account the values of the currents in these elements. Additionally, the Zero Voltage Switching (ZVS) condition has been introduced to penalize losses in the converter via $\Delta Arg(I_p)$. ZVS ensures that voltage drops to zero before the IGBT switches on or off, eliminating the overlap between voltage and current and minimizing losses. The above parameters are equal to 1 if any voltage, current, or phase shift values indicated in Table 6 exceed the maximum permissible value and are equal to 0 when they are below.

Finally, in Eq. (48), the constant K is a high-value parameter used to penalize solutions that fail to meet the constraints. Moreover, it is squared to prevent abrupt transitions. In the context of this study, $K = 2 \times 10^9$.

Table 6
Permissible limit values of circuit parameters.

Circuit values	Maximum($\leq$)
VC_{123} [kV]	3.5
VL_{ps3} [kV]	2
I_p [A]	40
I_{Lp} [A]	75
I_s [A]	60
$Arg(I_p)$ [°]	0

Subsequently, the value of the calculated primary and secondary resistance ($R_{ps,ij}$), the values of the three capacitors ($C_{123,ij}$), the inductance ($L_{3,ij}$), and the objective function value $J_{PD,ij}$ are added to each $y_{d,ij}$. This process yields the updated set $Y'_{d,i}$:

$$y\prime_{d,ij}\left(x_{d,i}, f_{ij}, V_{p,ij}, V_{s,ij}, R_{ps,ij}, C_{123,ij}, L_{3,ij}, J_{PD,ij}\right) =$$
$$y\prime_{d,ij}\left(y_{d,ij}, R_{ps,ij}, C_{123,ij}, L_{3,ij}, \ J_{PD,ij}\right) \in Y'_{d,i} \qquad (49)$$

After this step, the offspring $Y'd, i$ resulting from Step 2.2.4, which have been evaluated using the objective function, are combined with the parents $P_{d,i}$ (54) from Step 2.2.3, thereby upholding the principle of "elitism". The next equation represents this merging process:

$$Z_{d,i} = Y'_{d,i} \cup P_{d,i} \qquad (50)$$

Finally, the elements of $Z_{d,i}$ are sorted based on the value of their objective function $J_{PD,ij}$. The $jMax$ individuals with the lowest values of $J_{PD,ij}$ are selected, while the rest are discarded.

Evaluation of Iteration Continuity.

At the end of Step 2.2.2, the algorithm evaluates the iteration continuity based on three conditions. If any of these conditions are met, the algorithm terminates the iteration process and proceeds to Step 2.2.5; otherwise, it continues iterating and moves to Step 2.2.3.

- Condition 1: Maximum Number of Generations. If the number of generations exceeds the defined limit $Nmax_{GA}$, (Table 5) the algorithm terminates the iteration and proceeds to Step 2.2.5

$$Num \ gen_{AG} > Nmax_{GA} \qquad (51)$$

- Condition 2: Check of the Objective Function Value. If any of the objective function values $J_{PD,ij}$ is lower than the specified minimum $threshold J_{PD \ min} = 200$, the algorithm considers that there is at least one valid solution and finalizes the iteration proceeding to Step 2.2.5.

$$\min\left(J_{PD,ij}\right) < J_{PD \ min} \qquad (52)$$

- Condition 3: Comparison of Objective Functions Over Five Successive Iterations. By analyzing the results of $J_{PD,ij}$ from the last five iterations, an elitism counter (Elitism) increments each time the value of $J_{PD,ij}$ repeats. If this value repeats for five consecutive iterations, the algorithm deems it to have achieved the best possible result. The iteration finalizes and proceeds to Step 2.2.5.

If $\min\left(J_{PD,ij}\right) = J_{PD,ij \ NumgenGA-1}$,

$$\text{then } Elitism = Elitism + 1, \text{ else } Elitism = 1 \qquad (53)$$

Step 2.2.3 Selection of parents. The selection process uses a tournament-based selection method to choose Parents to generate the Offspring. In this process, pairs of individuals from Step 2.2.2, represented by $z_{d,ij} \in Z_{d,i}$, are randomly selected. Their objective function values $J_{PD,ij}$ are compared. The individual with the higher $J_{PD,ij}$ in each pair is eliminated, resulting in a set of $jMax/2$ selected parents $p_{Sd,ij} \in P_{Sd,i}$ for generating the offspring. The output of this step consists of two sets as follows:

- The set of parents $P_{d,i}$ which is sent to Step 2.2.2:

$$p_{d,ij} \in P_{d,i}; i = 1...iMax; j = 1...jMax. \qquad (54)$$

- The set of selected parents $P_{Sd,i}$ for generating the offspring, which is sent to Step 2.2.4:

$$p_{Sd,ij} \in P_{Sd,i}; i = 1...iMax; j = 1...jMax/2. \qquad (55)$$

Step 2.2.4 Obtaining offspring. A process of crossover and mutation generates the offspring. Each pair of selected parents from the previous step ($p_{Sd,ij} \in P_{Sd,i}$) undergoes crossover, resulting in initial offspring. Subsequently, a random selection process is employed to perform mutation on some of the offspring, producing the final offspring $o_{d,neratei,j} \in O_{di}$.

$$o_{d,i,j}\left(N_{ps,i}, S_{ps,i}, KC_{13,i}, L_{ps,i}, M_i, M_{max,i}, M_{min,i}, f_{ij}, V_{p,ij}, V_{s,ij}\right)$$
$$\in O_{di};$$
$$o_{d,i,j}\left(x_{d,i}, f_{ij}, V_{p,ij}, V_{s,ij}\right) \in O_{di}; i = 1...iMax; j = 1...jMax/2. \qquad (56)$$

The crossover operation is based on a Simulated Binary Crossover [14,42–44], which is applied to each pair of selected parents, resulting in two children c_i and c_{i+1}, using the following expression:

$$c_{ij}(k_l) = \frac{1}{2}((1 - \beta_k)p_{Sd,ij1}(k_l) + (1 + \beta_k)p_{Sd,ij2}(k_l)) \qquad (57)$$

$$c_{ij+1}(k_l) = \frac{1}{2}((1 + \beta_k)p_{Sd,ij1}(k_l) + (1 - \beta_k)p_{Sd,ij2}(k_l)) \qquad (58)$$

where k_l represents the crossover variables f, V_p, and V_s, whose limits are provided in Table 4. β is the spread factor, defined as the ratio of the dispersion of offspring values to that of the parent values. It is computed for each variable k_l according to the following expression [45]:

$$\beta = \begin{cases} (2u)^{\frac{1}{\eta_c+1}} & \text{if } u \leq 0.5 \\ \frac{1}{2(1-u)^{\frac{1}{\eta_c+1}}} & \text{if } u > 0.5 \end{cases} \qquad (59)$$

u is a random value ranging from 0 to 1, and η_c is the distribution index. In this paper, $\eta_c = 20$ is used, as it has demonstrated favorable results in a similar application [14,46–49].

The Mutation is derived by randomly altering the values of f, V_p and V_s in any of the children (c_i) using the following polynomial equation:

$$m_{i,j}(k_l) = p_{Sd,ij}(k_l) + (k_{l,max} - k_{l,min})\delta_k \qquad (60)$$

With $k_{l,max}$ and $k_{l,min}$ representing the maximum and minimum values of each optimization variable k_l, as defined in Table 4. δ is the distribution that governs the dispersion factor, which is calculated for each variable k_l as follows:

$$\delta = \begin{cases} (2r_k)^{\frac{1}{\eta_c+1}} & \text{if } r_k \leq 0.5 \\ 1 - (2(1-r_k))^{\frac{1}{\eta_c+1}} & \text{if } r_k > 0.5 \end{cases} \qquad (61)$$

Here r_k is a value sampled from a uniform distribution between 0 and 1, and $\eta_c = 20$ represents the distribution index.

Step 2.2.5 Obtaining the result. If any of the conditions of (51), (52) or (53) is met, the iterative process is terminated, and the individual with the lowest value of the objective function $J_{PD,ij}$ from (50) is selected. This is the best solution in Position 1, which is the nominal position:

$$s_{d,i}\left(N_{ps,i}, S_{ps,i}, KC_{13,i}, L_{ps,i}, M_i, M_{max,i}, M_{min,i}C_{123,ij}, L_{3,ij}, J_{PD,ij}\right)$$
$$= s_{d,i}\left(x_{d,i}, KC_{13,i}, \ C_{123,ij}, L_{3,ij}, J_{PD,ij}\right) \qquad (62)$$

This marks the end of GA1, sending this solution to Steps 2.3, 2.4, and 2.5.

6.2.3. Step 2.3 and Step 2.4. Check if the Position 1 solution works in Position 2 and Position 3 using genetic algorithms GA2 and GA3

The result from Step 2 of GA1 (62) represents the optimal solution for a primary and secondary coil in their nominal positions. Steps 3 and 4 aim to evaluate the performance of this solution when the coils are positioned in Position 2 and Position 3, respectively.

The process is the same for Phases 1 and 3, with the main difference being:

- Phase 1: In this phase, the inductances L_p and L_s remain constant regardless of the position, as (29) does not account for variations in the distance between the primary and secondary coils.
- Phase 3: This phase accounts for variations in L_p and L_s due to changes in the distance and air gap between the coils. Specifically, L_{pmin} and L_{smin} are considered in Position 2 (Step 2.3), while L_{pmax} and L_{smax} are taken into account in Position 3 (Step 2.4). These values were calculated in Phase 2 using (37).

Step 2.3.1 and Step 2.4.1 Random initialization of GA2 and GA3. In these steps, $jMax$ random values for f, V_p and V_s are added to the solution $s_{d,i}$ from (62). For Step 2.3.1 (GA2) and Step 2.4.1 (GA3), this results in:

$$Step\ 2.3.1\ (GA2): y_{min,ij}\left(s_{d,i}, f_{ij}, V_{p,ij}, V_{s,ij}\right) \in Y_{min,i}; i = 1...iMax;$$
$$j = 1...jMax \tag{63}$$

$$Step\ 2.4.1\ (GA3): y_{max,ij}\left(s_{d,i}, f_{ij}, V_{p,ij}, V_{s,ij}\right) \in Y_{max,i}; i = 1...iMax;$$
$$j = 1...jMax \tag{64}$$

$Y_{min,i}$ and $Y_{max,i}$ represent the sets of parents that will be evaluated in the next step of the genetic algorithm process.

Step 2.3.2 and Step 2.4.2 Calculation of circuit parameters and objective function. After the selection of parents in Step 2.3.1 for GA2 and Step 2.4.1 for GA3, the evaluation process begins. During the first iteration, parents are evaluated using the objective function (48) and restrictions in Table 6.

In GA2 it involves $y_{min,ij}$ from (63), and in GA3 it involves $y_{max,ij}$ from (64).

From the second iteration to the final one, the offspring $o_{min,ij} \in O_{min,i}$ from (75) in Phase 1 and the offspring $o_{max,ij} \in O_{max,i}$ from (76) in Phase 3 are evaluated, and these offspring are renamed:

$$Step\ 2.3.2\ (GA2): Y_{min,ij+1} = O_{min,ij} \tag{65}$$

$$Step\ 2.4.2\ (GA3): Y_{max,ij+1} = O_{max,ij} \tag{66}$$

The calculation of inductor resistances (R_{ps}) based on the frequency (f) is essential as the resistances depend on the frequency. This is done for each individual $y_{min,ij} \in Y_{min,i}$ in GA2 (from (63)) and each $y_{max,ij} \in Y_{max,i}$ in GA3 (from (64)). The values of capacitors $C_{123,ij}$ and coil $L_{3,ij}$ are not calculated again as they are part of the solution $s_{d,i}$ from (62).

Once the objective function (48) and its restrictions are evaluated, $J_{PDmin,ij}$ is obtained with GA2, and $J_{PDmax,ij}$ is obtained with GA3. This leads to the sets $y'_{min,ij} \in Y'_{min,i}$ for Step 2.3.2 and $y'_{max,ij} \in Y'_{max,i}$ for Step 2.4.2.

$$Step\ 2.3.2\ (GA2): For\ each\ y_{min,i}: y'_{min,ij}(y_{min,ij}, R_{ps,ij}, J_{PDmin,ij}) \in Y'_{min,i} \tag{67}$$

$$Step\ 2.4.2\ (GA3): For\ each\ y_{max,i}: y'_{max,ij}(y_{max,ij}, R_{ps,ij}, J_{PDmax,ij})$$
$$\in Y'_{max,i} \tag{68}$$

At the end of this step, the concatenation between $Y'_{min,i}$ and $P_{min,i}$ from Step 2.3.3 in the GA2 algorithm and between $Y'_{max,i}$ and $P_{max,i}$ from Step 2.3.4 in the GA3 algorithm is produced, which results in:

$$Step\ 2.3.2\ (GA2): Z_{min,i} = Y'_{min,i} \cup P_{min,i} \tag{69}$$

$$Step\ 2.4.2\ (GA3): Z_{max,i} = Y'_{max,i} \cup P_{max,i} \tag{70}$$

The set $Z_{min,i}$ obtained in GA2 includes both the parents generated in Step 2.3.3 and the offspring from Step 2.3.4. Similarly, the set $Z_{max,i}$ obtained in GA3 includes both the parents from Step 2.4.3 and the offspring from Step 2.4.4, ensuring the principle of "elitism" in both cases.

Lastly, in GA2, the elements of $Z_{min,i}$ are sorted based on their objective function $J_{PDmin,ij}$, selecting the $jMax$ individuals with the lowest values of $J_{PDmin,ij}$ and discarding the rest. The same process is applied in GA3 with the elements of $Z_{max,i}$ considering $J_{PDmax,ij}$.

Evaluation of the Continuity Condition

Both algorithms, GA2 and GA3, include the same conditions as GA1 ((51), (52) and (53)) to determine whether to continue iterating in Step 2.3.3 and 2.4.3, respectively or to finalize the process and proceed to Step 2.3.5 or 2.4.5 in each case.

Step 2.3.3 and Step 2.4.3 Selection of parents. The selection tournament is the same as the one described in GA1, tailored for each algorithm, GA2 and GA3.

The output of this step consists of:

- The set of parents sent to Step 2.3.2 in the case of GA2 or Step 2.4.2 in the case of GA3:

$$Step\ 2.3.3\ (GA2): p_{min,ij} \in P_{min,\ i}; i = 1...iMax; j = 1...jMax \tag{71}$$

$$Step\ 2.4.3\ (GA3): p_{max,ij} \in P_{max,\ i}; i = 1...iMax; j = 1...jMax \tag{72}$$

- The set of selected parents for generating the offspring sent to Step 2.3.3 or Step 2.4.3 in the case of GA2 and GA3, respectively:

$$Step\ 2.3.3\ (GA2): p_{Smin,ij} \in P_{Smin,i}; i = 1...iMax; j = 1...jMax/2 \tag{73}$$

$$Step\ 2.4.3\ (GA3): p_{Smax,ij} \in P_{Smax,i}; i = 1...iMax; j = 1...jMax/2 \tag{74}$$

Step 2.3.4 and Step 2.4.4 Obtaining offspring. The process of obtaining offspring is the same as explained in 2.2.4.

$$Step\ 2.3.4\ (GA2): o_{min,i,j}\left(s_{d,i}, f_{ij}, V_{p,ij}, V_{s,ij}\right) \in O_{min,i};$$
$$i = 1...iMax; j = 1...jMax/2. \tag{75}$$

$$Step\ 2.4.4\ (GA3): o_{max,ij}\left(s_{d,i}, f_{ij}, V_{p,ij}, V_{s,ij}\right) \in O_{max,i}; i = 1...iMax;$$
$$j = 1...jMax/2. \tag{76}$$

Step 2.3.5 and Step 2.4.5 Obtaining the result. Similar to Step 2.2.5, when any of the conditions in (51),(52) or (53) is met, the iterative process stops. The final solution for each algorithm is then selected by choosing the element from (69) for GA2 and (70) for GA3, with the lowest value of the objective function, $J_{PDmin,i}$ for GA2 and $J_{PDmax,i}$ for GA3, respectively.

$$Step\ 2.3.5\ (GA2): s_{min,i}(s_{di}, J_{PDmin,i}) \tag{77}$$

$$Step\ 2.4.5\ (GA3): s_{max,i}(s_{di}, J_{PDmax,i}) \tag{78}$$

These solutions are then sent to Step 2.5, concluding the process of GA2 and GA3.

6.2.4. Step 2.5: Calculation of NSGA-II objective functions

In Step 2.5 the algorithm receives three solutions from GA1 (62), GA2 (77), and GA3 (78). For each iteration of the counter i: $s_{d,i}$, $s_{min,i}$, and $s_{max,i}$ share the same values as follows:

- In Phase 1, they share the same values of N_{psi}, $S_{ps,i}$, $KC_{123,i}$, $L_{ps,i}$, M_i, $M_{max,i}$, $M_{min,i}$, $C_{123,i}$, $L_{3,i}$.
- In Phase 3, they share the same values of $S2$ (40), $KC_{123,i}$, $C_{123,i}$, $L_{3,i}$.

Each set of three solutions for i is integrated into one: $s_{t,i} = s_{d,i} \cup s_{min,i} \cup s_{max,i}$, obtaining the solution of Phase 1 (79) and Phase 3 (80).

$$s_{t,i}\left(N_{ps,i}, S_{ps,i}, KC_{123,i}, L_{ps,i}, M_i, M_{max,i}, M_{min,i}, C_{123,i}, L_{3,i}, J_{PD,i},\right.$$
$$\left. J_{PDmin,i}, J_{PDmax,i}\right)$$
$$= s_{t,i}\left(s_{d,i}, J_{PDmin,i}, J_{PDmax,i}\right) \in S_t \tag{79}$$

$$s_{t,i}\left(S2, KC_{13,i}, C_{123,i}, L_{3,i}, J_{PDd,i}, J_{PDmin,i}, J_{PDmax,i}\right)$$
$$= s_{t,i}\left(s_{d,i}, J_{PDmin,i}, J_{PDmax,i}\right) \in S_t \tag{80}$$

The objective functions of the NSGA-II algorithm for each phase are now evaluated for every individual in S_t.

Phase 1. Objective functions:

The Objective functions for Phase 1 (81) and (82) are the same as those explained in [14] The objective is to minimize the volume of copper used in the primary coil (Vol_{cup}) and in the secondary coil (Vol_{cus}), considering the three scenarios explained in Section 5.

$$Jcu_p = Vol_{cup} + K^2(J_{PD} + \Delta Eff + \Delta \delta I_{Lp} + \Delta \delta I_s) + K(J_{PDmax} + J_{PDmin}) \tag{81}$$

$$Jcu_s = Vol_{cus} + K^2(J_{PD} + \Delta Eff + \Delta \delta I_{Lp} + \Delta \delta I_s) + K(J_{PDmax} + J_{PDmin}) \tag{82}$$

where Vol_{cu} for each coil is calculated as:

$$Vol_{cu} = \frac{d_0^2}{4} \pi n_t N 2(a+b) \tag{83}$$

Here, a and b are the average coil size, n_t is the number of strands of each coil, and d_0 is the strand diameter. The optimal strand diameter for a working frequency between 79 and 90 kHz is 0.1 mm [38]. Obtaining:

$$s_{C,i}(N_{ps,i}, S_{ps,i}, KC_{13,i}, L_{ps,i}, M_{d,i}, M_{max,i}, M_{min,i}, C_{123,i}, L_{3,i}, Jcu_{ps,i}) =$$
$$s_{C,i}(sd, i, Jcups, i) \in S_C \tag{84}$$

Phase 3. Objective functions:

The objective of Phase 3 is to obtain the optimal capacitor values. The system behavior depends on the relationship between capacitors C_1 and C_3, related by KC_1 and KC_3, as demonstrated in Section 2. Therefore, the objective is to optimize both parameters considering the three scenarios explained in Section 5.

$$J_{KC1} = KC_1 + K^2(J_{PD} + \Delta Eff + \Delta \delta I_{Lp} + \Delta \delta I_s) + K(J_{PDmax} + J_{PDmin}) \tag{85}$$

$$J_{KC3} = KC_3 + K^2(J_{PD} + \Delta Eff + \Delta \delta I_{Lp} + \Delta \delta I_s) + K(J_{PDmax} + J_{PDmin}) \tag{86}$$

Obtaining:

$$s_{C,i}(s_{d,i}, J_{KC1,i}, J_{KC3,i}) = s_{C,i}(s_{d,i}, J_{KC13,i}) \in S_C \tag{87}$$

The objective functions of both phases include several penalizations to ensure the design meets certain criteria. These include:

- Efficiency penalization (ΔEff): A penalty is applied if the efficiency in the central position is less than 99%. In this case, ΔEff equals 1; otherwise, its value is 0.
- Current density penalization ($\Delta \delta I_{Lp}$ and $\Delta \delta I_s$): If the current density in any of the inductors exceeds 3 A/mm² [41], a penalty is applied. If either density is exceeded, $\Delta \delta I_{Lp}$ or $\Delta \delta I_s$ equals 1; otherwise, they remain at 0.

- Power penalization in Position 1 (J_{PD}): This penalty favors designs with higher power efficiency in the central position, resulting in lower J_{PD} values.
- Power penalization in Position 2 (J_{PDmin}) and Position 3 (J_{PDmax}): The results of the optimization functions of the GA2 and GA3 algorithms are also considered.

The first three penalizations are multiplied by the factor K^2, while the last is multiplied by the factor K. This approach ensures that if a specific design can deliver full power in the centered position while also meeting efficiency and current density requirements, it is not discarded, even if the power in extreme positions is not ideal but close to it.

6.3. Step 3. Evaluation of solutions

This step involves evaluating the set of solutions to identify the best results. It consists of two fundamental processes: the Non-dominance test and Crowding distance evaluation. The Non-dominance test categorizes the solutions into different Pareto-Optimal Sets, while the Crowding distance is used to assess the solutions within the same Pareto-optimal set.

Once Step 3 is completed, a validation check determines if the maximum number of generations has reached the defined limit $Nmax_{GA}$ (Table 5). If this condition is unmet, the data proceeds to Step 4, and the iterative procedure continues. On the other hand, the desired Pareto Front is obtained, and the algorithm proceeds to Step 6.

6.3.1. Step 3.1 Non-dominance test

In the context of a multi-objective optimization problem, the quality of a solution is determined by the concept of dominance. The Non-dominance test, utilized during Step 2.5, evaluates and compares the obtained results based on this principle. One solution is considered superior to another if it meets the following conditions [50]:

- Solution x_1 is not worse than x_2 in all objectives.
- Solution x_1 is strictly better than x_2 in at least one objective.

The dominance test is performed iteratively for each individual in the solution set, generating a set of non-dominated solutions. This set comprises all solutions that are not dominated by any other member of the solution set in terms of their objectives. The non-dominated set within the feasible decision space is referred to as the Pareto-Optimal Set, and the boundary defined by the collection of all mapped points of the Pareto-Optimal Set is known as the Pareto-Optimal Front.

This iterative process continues until all population members have been categorized into different Pareto fronts.

6.3.2. Step 3.2: Determine crowding distance

In this step, the solutions within each Pareto front are ordered based on their Crowding distance. The Crowding distance is calculated as the Euclidean distance between each solution in the same Pareto front. This distance is determined as a function of the Objective Functions. To ensure that solutions located at the extremes of the front are not discarded, infinite distance is assigned to them.

The equation that defines the Crowding distance is as follows:

$$d_{X,i} = \sum_{m=1}^{2} \left| \frac{J_m(x_{i+1}) - J_m(x_{i-1})}{(J_m^{max} - J_m^{min})} \right| = \left| \frac{J_p(x_{i+1}) - J_p(x_{i-1})}{(J_p^{max} - J_p^{min})} \right|$$
$$+ \left| \frac{J_s(x_{i+1}) - J_s(x_{i-1})}{(J_s^{max} - J_s^{min})} \right| \tag{88}$$

Where:

- J_m^{max} and J_m^{min} represent the maximum and minimum values of the Objective Functions.
- $J_m(x_{i+1})$ and $J_m(x_{i-1})$ are the Objective Function values of the neighboring solutions to x_i, for each objective function: Jcu_p (81) and Jcu_s (82) for the Phase 1, and J_{KC1} (85) and J_{KC3} (86) for the Phase3.

6.4. Step 4: Tournament selection

In this step, two comparisons are made:

- First: The selection of the solution located in the best Pareto Set.
- Second: If the solutions belong to the same Pareto Set, the largest crowding distance is used to determine the predominant solution.

The set of solutions obtained is the set of Parents, denoted as $p_{C,i} \in P_C$, where:

$$Phase\ 1 : p_{C,i}\left(N_{ps}, S_{ps}, KC_{13}\right); p_{C,i} \in P_C \tag{89}$$

$$Phase\ 3 : p_{C,i}\left(S2, KC_{13}\right); p_{C,i} \in P_C \tag{90}$$

The set of Parents is then sent to Step 3 and Step 5 to obtain the Offspring.

6.5. Step 5: Obtaining offspring

The set of elements belonging to the Offspring ($o_i \in O$)is obtained from the union of the individuals obtained by Crossover ($c_i \in C$) in Step 5.1 and a process of Mutation ($m_i \in M$) in Step 5.2, from the parents P_C of Step 4.

$$O = C \cup M \tag{91}$$

The variables that are crossed and mutated are:

- Phase 1: N_{ps}, S_{ps} and KC_{13}.
- Phase 3: KC_{13}.

Unlike the method used in GA1, GA2, and GA3, where the mutation is applied to the offspring randomly, in this case, the mutation is applied directly to the parent population.

The set of Offspring is then sent to Step 2, and from there, it is sent to Step 3, where it will be evaluated together with the parents from Step 4.

6.5.1. Step 5.1 Crossover

The same SBX process as explained in Step 2.2.4 is performed using (57)–(59) to obtain the Crossover offspring: $c_i \in C$.

6.5.2. Step 5.2 Mutation

The same mutation process of Step 2.2.4 using (60) and (61) is employed to obtain Mutation offspring ($m_i \in M$). The distinction lies in the fact that, in this case, the mutation is applied to the parents (P_C) rather than to the Crossed offspring

6.6. Step 6 Final pareto front and solution selection

At the end of Step 3, the number of iterations is checked. If it reaches the limit, the NSGA-II algorithm stops and proceeds to Step 6. In this Step, the results are plotted, generating a Pareto front in each Phase: Fig. 5 in the case of Phase 1, Fig. 6 in the case of Phase 3. Now, the final solution can be selected.

Selection of the Phase 1 Solution ($S1$):

In the case of Phase 1, the objective functions, (81) and (82), aim to minimize the amount of copper required in the primary and secondary inductors, respectively. Three Scenarios are defined:

- Scenario 1: Minimization of the copper volume of the ground coil.
- Scenario 2: Minimization of the volume of the on-board coil.
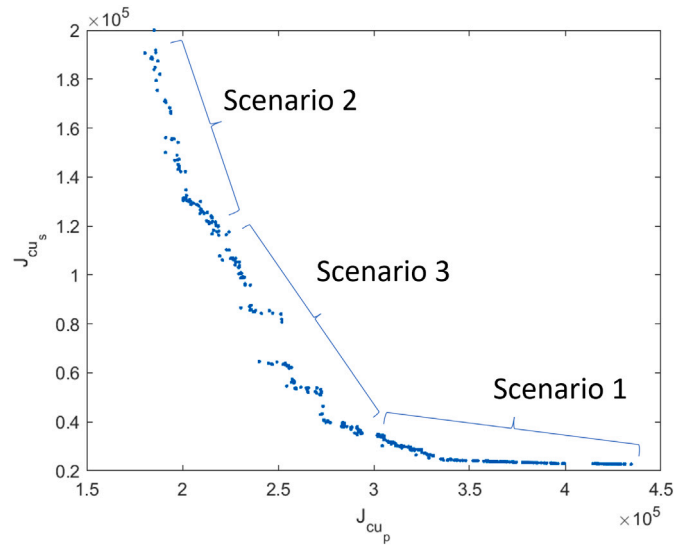- Scenario 3: Compromise solution that minimizes both.

Fig. 5. Pareto-front and scenarios of Phase 1.

Since the objective of this paper is to minimize the global price, Scenario 3 is chosen.

The analysis of the results obtained in Scenario 3 leads to the conclusion that there is a set of solutions in which the amount of copper is very similar. Still, they have quite different currents, always within the defined limits of Table 6. To select among these cases, the solution involving maximum mutual inductance (M) is sought. Increasing M results in less current required in the primary inductor (I_{Lp}), thereby reducing the value of C_1.

The process for choosing the final solution in Phase 1 consists of the following steps:

- Search for the Solution $S1_{JcuTmin}$ with the minimum value of $Jcu_T = Jcu_p + Jcu_s$.
- Select the solutions from Scenario 3 whose value of Jcu_T differs by less than 10% from that of $S1_{JcuTmin}$.
- Order these solutions from highest to lowest M.
- Select the solution with the highest M, which becomes the final solution of Phase 1: $S1$.

The result of this phase is a single defined individual $S1$ (39), which provides the initial approximate values for:

- The number of turns: N_p for the primary and N_s for the secondary.
- The cross-section: S_p for the primary and S_s for the secondary.
- Inductances: L_p for the primary and L_s for the secondary.
- Mutual inductance in three positions: M, M_{max}, and M_{min}.

Table 7 shows the values obtained for the solutions $S1_{JcuTmin}$ and $S1$.

The values of the objective functions Jcu_p and Jcu_s represent directly the volume of copper used in the primary and the secondary, respectively. As can be observed, the total copper volume (Jcu_T) of $S1$ is 1,45% greater than that used in $S1_{JcuTmin}$. However, when analyzing the performance (Table 8), it is evident that the current in the primary winding, I_{Lp}, in solution $S1$, is 35.61% lower. Hence, $S1$ is chosen as the solution for Phase 1.

Therefore, $S1$ is subjected to analysis in Phase 2 using a 3D finite element program, in which ferrite and aluminum are incorporated. This analysis yields $S2$ (40) with the final values of the previously

Table 7
Results of $S1_{JcuTmin}$ and $S1$ of Phase 1.

Parameter	$S1_{JcuTmin}$	$S1$
N_p	12	12
N_s	12	18
S_p [mm²]	19.75	14.79
S_s [mm²]	8.11	11.52
L_p [µH]	162.09	173.9
L_s [µH]	116.9	189.23
M [µH]	34.7	43.6
M_{max} [µH]	40.75	50.02
M_{min} [µH]	25.31	33.39
Jcu_p [cm³]	247.68	187.48
Jcu_s [cm³]	68.439	133.23
Jcu_T [cm³]	316.12	320.71

Table 8
Comparison of currents for solutions $S1_{JcuTmin}$ and $S1$ in Phase 1.

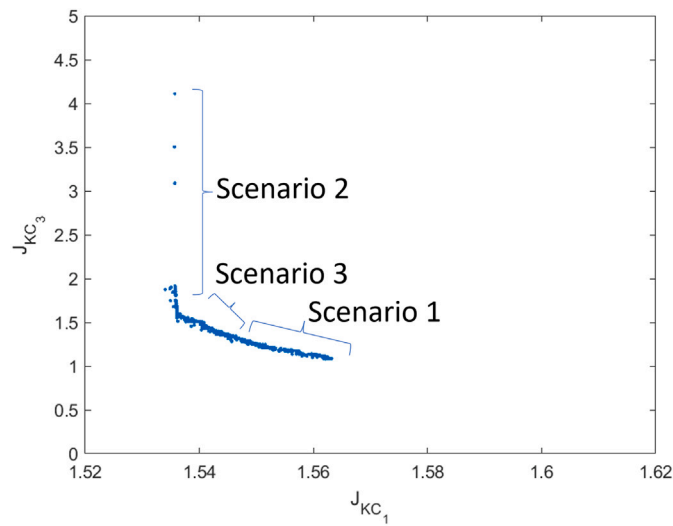|	I_p	I_{Lp}	I_s
$S1_{JcuTmin}$	16.69	29.2	19.65
$S1$	17.07	21.53	22.38

Fig. 6. Pareto-front and Scenarios for Phase 3.

mentioned parameters and the values of the inductances L_p and L_s in the three defined positions.

Selection of the Phase 3 Solution ($S3$):

For Phase 3, the selection of Scenario 3 is also based on the objective functions (85) and (86), which aim to minimize the values of KC_1 and KC_3 respectively. As in the case of Phase 1, three scenarios are defined depending on the behavior of the system:

- Scenario 1: The system tends toward S–S behavior.
- Scenario 2: The system leans toward P–S behavior.
- Scenario 3: Represents intermediate behavior.

Fig. 6 shows the Pareto front and scenarios for Phase 3.

As explained in Section 2, to leverage the advantages of both topologies, S–S and P–S, Scenario 3 is selected in this paper. Then, from this Pareto front, the solution with the lowest value of $J_{KCT} = J_{KC1} + J_{KC3}$ is selected.

This result reduces the capacitance of C_1, C_3, and consequently L_3, resulting in a more cost-effective solution for the compensators. The obtained result, $S3$ (41), represents the optimized outcome of the entire process. Its key parameters can be found in Table 7, with the values of the number of turns, cross-sections, inductances, and mutual inductance obtained from the Phase 2 result.

Phase 3 allows obtaining not only the values of the components of the circuit from Table 9 but also the values of the voltages V_p, V_s, and frequency f required to transfer the target power P_D with maximum efficiency. Table 10 shows these values in each position.

Convergence Analysis of an NSGA-II Algorithm Nested with Three GAs

The performance of multi-objective algorithms can be evaluated in various ways. [51–55] propose, among others, visual inspection of the Pareto front and hypervolume. Visual inspection reveals generated solutions' distribution, dispersion, and quality, providing insights into algorithm convergence and its ability to find optimal solutions. Simulations are conducted with different population sizes and generations to assess this. Hypervolume provides a quantitative measure of the quality of the Pareto front. Higher hypervolume indicates better coverage and diversity of solutions.

Both methods have been applied to the NSGA-II algorithms with three nested genetic algorithms developed in Phases 1 and 3 to validate the algorithm's performance. Five simulations were performed with the same number of individuals in the population and generations, and the hypervolume was calculated, selecting the one with the best value. Then, the number of individuals in the population and the number of generations were increased, and the calculation was repeated. This process was carried out until a satisfactory result was obtained from a given number of individuals in the population and for different generations.

Fig. 7 displays the Pareto fronts obtained with different combinations of populations and generations. It can be observed that the Pareto front obtained with 500 individuals in the population and 100 generations yields similar results to those obtained with 600 individuals in the population and 120 generations, confirming algorithm convergence.

Furthermore, Tables 11 and 12 illustrate the evolution of hypervolume and computation time for the same cases depicted in the figure. Results show that hypervolume increases with the number of populations and generations, indicating algorithm convergence. Additionally, computation time increases, although all times obtained in the simulations were low.

7. Phase 2: Optimal design of the complete system

Phase 2 receives the solution $S1$ from Phase 1, where ideal conditions were assumed, neglecting ferrites and aluminum shielding, and where the variation in primary (L_p) and secondary (L_s) inductance values due to changes in primary and secondary positions cannot be obtained. In this phase, a 3D finite element program is used to fully design the windings, including ferrites and shielding, ensuring compliance with the magnetic field limitation defined by ICNRIP 2010 [56] in all positions, and obtaining the values of L_p, L_s (37) and M (38) in the three design positions.

Since the solution $S1$ from Phase 1 is optimal, the goal of Phase 2, when adding ferrites and aluminum, is to achieve a system that maintains inductance and mutual inductance values as close as possible to those of $S1$.

To achieve this, the test platform described in the SAE J2954 Standard [13] is first drawn, as seen in Fig. 8. It consists of the following parts:

- The inductors.
- Ferrite in both inductors.
- Shielding, made up of three aluminum sheets. The first is on the primary, the second is attached to the secondary inductor, and the third is on the vehicle.
- Ferromagnetic sheet, which simulates the bottom part of the vehicle.

Table 9
Final result (*S*3) of Phase 3.

N_p	N_s	S_p [mm²]	S_s [mm²]	KC_1	KC_3	C_1 [nF]	C_2 [nF]	C_3 [nF]	L_3 [µH]
12	18	19.75	8.11	1.5323	1.5514	40.496	18.964	75.163	46.93

Table 10
Values of the voltages V_p, V_s and frequency f required in the three positions.

Position	V_p [V]	V_S [V]	f [kHz]
Position 1	678.76	708.71	83.641
Position 2	640.51	370.39	89.999
Position 3	672.5	780.91	80.224

Table 11
Hypervolumen analysis for the NSGA-II + 3GAs of Phase 1.

Pop	Gen	Hypervolumen	Time [s]
100	20	0.1684	148.52
200	40	0.2182	525.22
300	60	0.238	1177.19
400	80	0.3387	2209.3
500	100	0.4804	2752.4
600	120	0.4635	3839.65

Table 12
Hypervolumen analysis for the NSGA-II + 3GAs of Phase 3.

Pop	Gen	Hypervolumen	Time [s]
100	20	0.0285	189.42
200	40	0.0292	691.47
300	60	0.0269	1461.65
400	80	0.0379	2689.34
500	100	0.0341	4177.29
600	120	0.0348	6198.10

This platform is the basis for designing the inductors and individual components and modifying component sizes and distances. In contrast to the standard results for WPT2 and WPT3, the ferrite layer is designed to consist of a single sheet, reducing the number of ferrites and simplifying manufacturing, thus reducing costs.

For component modeling, the following simplifications are made:

- Inductors are modeled with uniform current density, with the same number of turns as obtained in Phase 1.
- The surface occupied by the ferrites is square, exceeding the coil width by five millimeters, with a central window.
- The thickness of the ferrites is selected according to the SAE J2954 standard.
- The type of ferrite used is the Ferroxcube 3C90 [57], commonly used in household heating systems and cost-effective, with characteristics similar to those defined in the SAE J2954.
- In the search for the final solution, the aim is to ensure that the inductance values obtained are as close as possible to those obtained in Phase 1.

Ferrite geometry and the distance between components are optimized using a parametric sweep. This optimization involves discretizing the size of the ferrites and distances to carry out a series of sweeps, allowing the identification of combinations that achieve results closest to the Phase 1 solution, considering the worst-case scenarios for mutual inductance:

- Position 2: Maximum mutual inductance.
- Position 3: Minimum mutual inductance.

From among the best options found, the solution *S*2 (40) that minimizes the ferrite size is selected and sent to Phase 3. The results are shown in Table 13. As seen, the number of turns from Phase 1 has been maintained.
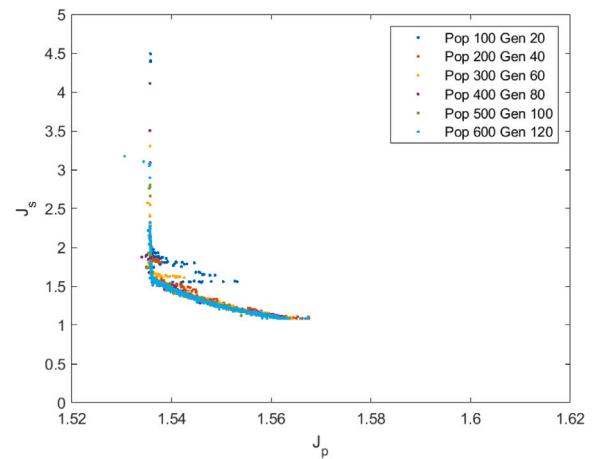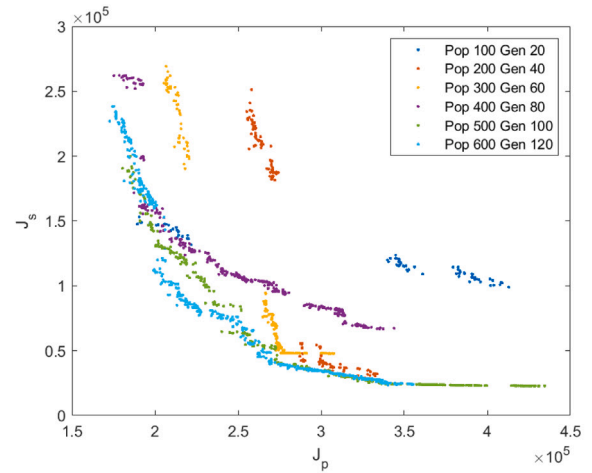

(a) Phase 1

(b) Phase 3

Fig. 7. Pareto sets obtained for different numbers of individuals in Population and Generations for the NSGA-II + 3GA in Phase 1 and Phase 3.

Table 13
Comparison of parameters from Phase 1 and Phase 2.

Parameter	Phase 1 *(S1)*	Phase 2 *(S2)*
N_p	12	12
N_s	18	18
S_p [mm²]	14.79	19.75
S_s [mm²]	11.52	8.11
L_p [µH]	173.9	136.41
L_{pmax} [µH]	–	134.37
L_{pmin} [µH]	–	143.84
L_s [µH]	189.23	190.1
L_{smax} [µH]	–	199.36
L_{smin} [µH]	–	177.11
M [µH]	43.6	50.13
M_{max} [µH]	50.02	59.91
M_{min} [µH]	33.39	29.11
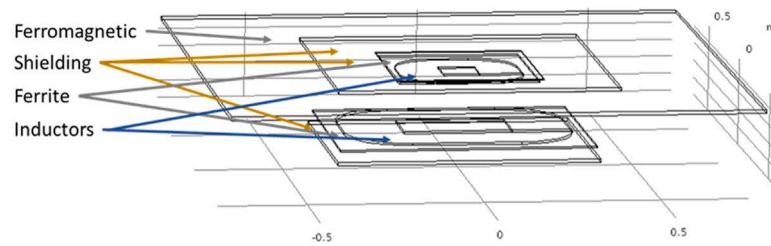
Fig. 8. Test platform designed according to SAE J2954.

(a) Position 1

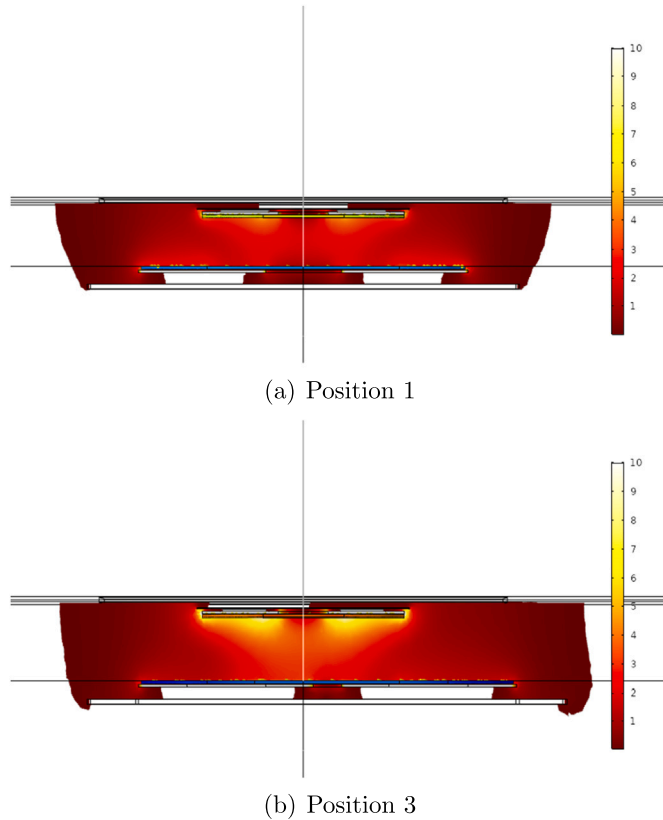(b) Position 3

Fig. 9. Electromagnetic field.

Even having included the ferrite and the shielding, the values of M and L_s have been successfully maintained practically the same. However, the value of L_p in Phase 2 is higher.

Finally, throughout the design process, it is confirmed that the value of the magnetic field emitted at any position complies with the required limits, as observed in Fig. 9 for Position 1 and Position 3.

Furthermore, all the essential parameters for its fabrication are obtained, including:

- The size of the ferrite core.
- Distances between ferrite cores and conductors.
- Distances between ferrite cores and aluminum shielding.

8. Validation of results

Prototypes for primary and secondary coils were manually fabricated for validation as seen in (Fig. 10). They have specific construction limitations, mainly due to material constraints and the complexities associated with the manual manufacturing process.

As seen in Fig. 10, achieving a design with uniformly distributed turns was not possible, and the availability of materials for the coils
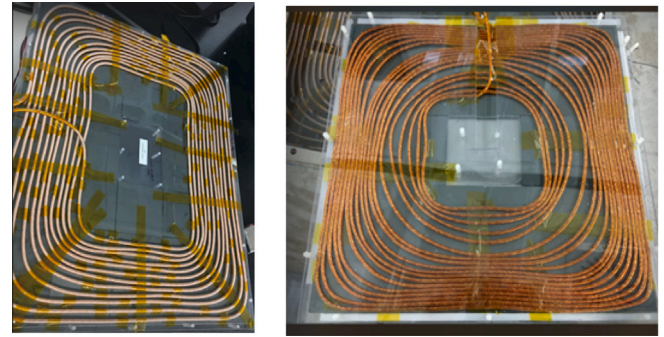
(a) Detail of the primary coil

(b) Detail of the secondary coil

Fig. 10. Detail of the constructed primary and secondary coils.

necessitated using sections that were slightly different from the ideal design. Furthermore, the exact distances between ferrites and coils as those obtained in the optimal Phase 2 design were not achieved.

8.1. Inductance verification

The results obtained from simulating the inductors in Phase 2, including ferrites and shielding, have been compared with those obtained through measurements of the coils manufactured using a GW INSTEK LCR 6300 measurement equipment. The results at various positions and heights are shown in Table 14.

In Table 15, the relative error in the simulation compared to the values measured in the prototype is shown.

It is observed that, despite the experimental design not being identical to the theoretical design, the results are very similar, especially in the centered position. The error is more significant in the off-center position because the model considers the inductor to have a homogeneous current density. In contrast, the coils finally fabricated were handmade with areas of higher current density than others due to the non-uniform winding of turns, especially in the secondary coil.

8.2. Validation of performance

The results obtained through the use of equations have been verified with a Matlab-Simulink model [14,58,59] of the system in different positions, as well as through experimental tests, the results of which can be seen in Table 16.

The coils were tested in the laboratory (Fig. 11) by supplying the primary with a power electronics configuration at two different airgap distances and three misalignment positions, conducting six tests. The electronic configuration used is an initial version with limitations in adjusting control parameters, so in all cases, $V_p = 800$ V and $f = 85$ kHz had to be used. Moreover, to optimize performance using the actual inductance values, the circuit compensators have been adjusted as follows: $C_1 = 37.6$ nF; $C_2 = 19.83$ nF; $C_3 = 70.5$ nF; $L_3 = 49$ μH.

Table 14
Inductance values from Phase 2 and values measured on the prototype.

Position	L_p Exp [µH]	L_s Exp [µH]	M Exp [µH]	L_p FEM [µH]	L_s FEM [µH]	M FEM [µH]
Pos 1	135.24	189.66	13.61	136.41	190.10	50.13
Pos 2	135.00	195.00	15.00	134.37	199.37	59.91
Pos 3	140.18	182.59	10.60	143.84	177.11	29.11

Table 15
Comparison of results in Table 14.

Position	Error L_p [%]	Error L_s [%]	Error M [%]
Pos 1	0.87	0.23	0.21
Pos 2	0.47	2.24	2.67
Pos 3	2.61	3.00	5.43

Fig. 11. Experimental test bench.

Table 16
Result of the values obtained through equations, simulation, and experimental testing.

Pos	Test	Vs [V]	I_p [A]	I_s [A]	P_p [kW]	P_s [kW]	Eff [%]
1	Exp	778.8	13.78	13.63	11.023	10.613	96.28
1	Sim	778.8	17.73	12.57	11.023	10.878	97.44
1	Eq	778.8	13.89	12.59	9.247	9.064	98.03
3	Exp	476.3	13.81	21.98	11.046	10.473	94.81
3	Sim	476.3	16.05	22.07	10.863	10.585	97.44
3	Eq	476.3	13.3	20.07	9.045	8.743	96.66

The differences observed in the table are primarily due to two reasons. Firstly, the values of the inductances and compensation circuit components used in the equations and the Matlab-Simulink simulation are those obtained in Phase 3 (Table 9), which are slightly different from those of the experimental setup. Secondly, due to the limitations of the power electronics, for a more realistic comparison in both equation modeling and Matlab-Simulink simulation, consistent values have been maintained across all cases, with $V_p = 800$ V and $f = 85$ kHz, albeit not corresponding to the optimal values derived in Phase 3 (refer to Table 10), consequently, the target power P_D is not achieved, particularly in equation-based modeling.

Fig. 12(a) and (b), obtained with the oscilloscope, represent in the upper part the value of V_p in blue, with 250 V/$division$, and I_p in gray. At the bottom, I_{Lp} in green, and I_s in pink, for Position 1 and Position 3, respectively. It can be seen that the waveform of the primary current (I_p) is not sinusoidal, although it is sinusoidal in the two inductor coils.

9. Conclusions

The paper presents a comprehensive methodology for the optimal design of an 11 kW WPT3 Z1 LCC-S system in compliance with SAE J2954 [13]. The process is developed in three phases, each building on the previous one, gradually increasing in complexity and allowing holistic optimization of the complete system.

Phase I focuses on the simplified system comprising only the coils and compensation circuit components, excluding ferrite and shielding.

Mathematical equations are used for the electromagnetic modeling of the inductor coils, allowing them to be included in a designed multi-objective NSGA-II algorithm, facilitating iterative calculations and reducing the required computation time. This algorithm optimizes local solutions in three different positions by nesting three genetic algorithms (GA1, GA2, and GA3) and including a set of design and performance constraints. This ensures the system will operate correctly at any misalignment and air gap position. The three positions are:

- Position 1: Centered and maximum height, allowing for the determination of nominal or design mutual inductance: M.
- Position 2: Centered and minimum height, allowing for determining maximum mutual inductance: M_{max}.
- Position 3: Maximum misalignment and maximum height, allowing for the determination of minimum mutual inductance: M_{min}.

The NSGA-II genetic algorithm developed employs two opposite objective functions, resulting in three optimization scenarios that allow the designer to choose between minimizing copper in the primary winding, minimizing copper in the secondary winding, or minimizing the total copper used. In this work, the solution corresponding to the third scenario is chosen. This scenario has a set of solutions with very similar copper volumes and slight differences in behavior. Therefore, a second selection process is applied among those solutions with a copper volume no more significant than 10% of the optimal theoretical solution, selecting the solution with the maximum mutual inductance (M). This reduces the current in the primary inductor (I_{Lp}) and, therefore, the value of C_1 and L_3, lowering the cost of both components.

In Phase 2, a detailed 3D finite element electromagnetic modeling is employed to design the inductor system based on the data obtained in Phase 1. This phase includes ferrites and aluminum shielding, providing final values of inductances L_p and L_s and the mutual inductance M for the three Positions, along with comprehensive manufacturing details.

Phase 3 uses the data from Phase 2 for the final optimal computation of the compensation circuit elements. Another NSGA-II genetic algorithm has been designed that also nests three local search genetic algorithms at each of the three positions and a set of design and performance constraints. This algorithm uses two opposite objective functions to obtain three decision scenarios: minimize KC_1, making the system behave as an S–S; minimize KC_3, making it behave as a P–S; or minimize both simultaneously, looking for an intermediate behavior. The chosen solution, corresponding to Scenario 3, while achieving the combined advantages of an S–S and P–S system, minimizes the combined cost of C_1, C_3, and L_3. The values of the voltages and frequencies with which the system electronics must be controlled to obtain the desired power with maximum efficiency are also obtained from this phase.

From the outset, this approach ensures that the designed system works in the central position and the other two positions defined by the standard, thus guaranteeing its performance in any intermediate position. This represents an improvement over the reviewed literature, where the design is typically performed only for the nominal position and subsequently tested for performance in other positions. A remarkable aspect of the work is that it combines two different methodologies in electromagnetic analysis: equations in the genetic algorithms, reducing computational costs, and FEM for shielding design, obtaining values very close to the real ones.

Validation of the results is carried out rigorously. The theoretical results of Phase 2 are compared with the measured values of
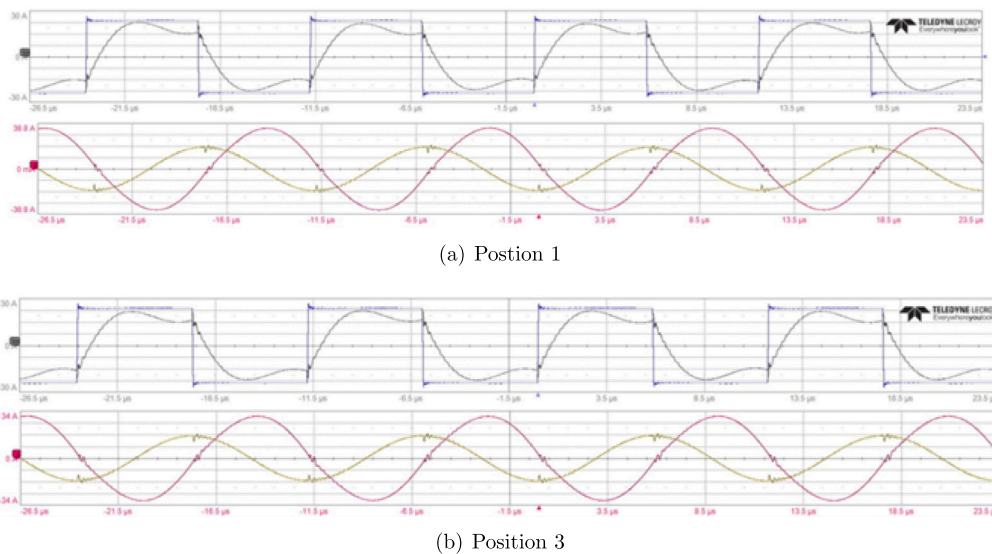
(a) Postion 1

(b) Position 3

Fig. 12. Waveform obtained with the oscilloscope for Vp (blue), Ip (gray), ILp (yellow), and Is (pink) at different positions.

the fabricated coils, showing slight differences. In addition, the system performance is verified by comparing the results obtained from equations with a Matlab-Simulink model and an experimental setup, demonstrating consistent results.

This adaptive procedure can be applied to other WPT designs with minor adaptations. Depending on the desired topology, it will be necessary to adjust the circuit equations to the desired topology, select the optimization parameters and their constraints, and adapt the objective functions of the genetic algorithms, if necessary.

CRediT authorship contribution statement

O. García-Izquierdo: Writing – review & editing, Writing – original draft, Validation, Supervision, Software, Methodology, Investigation, Formal analysis, Conceptualization. **J.F. Sanz:** Writing – review & editing, Writing – original draft, Validation, Supervision, Project administration, Methodology, Formal analysis. **J.L. Villa:** Writing – original draft, Validation, Supervision, Project administration, Formal analysis. **G. Martin-Segura:** Validation, Supervision.

Declaration of competing interest

The authors declare that they have no known competing financial interests or personal relationships that could have appeared to influence the work reported in this paper.

Data availability

No data was used for the research described in the article.

Acknowledgments

References

[1] Sallan J, Villa JL, Llombart A, Sanz JF. Optimal design of ICPT systems applied to electric vehicle battery charge. IEEE Trans Ind Electron 2009;56(6):2140–9. http://dx.doi.org/10.1109/TIE.2009.2015359.

[2] Villa JL, Sallán J, Llombart A, Sanz JF. Design of a high frequency Inductively Coupled Power Transfer system for electric vehicle battery charge. Appl Energy 2009;86(3):355–63. http://dx.doi.org/10.1016/j.apenergy.2008.05.009.

[3] Yang J, Zhang X, Zhang K, Cui X, Jiao C, Yang X. Design of LCC-S compensation topology and optimization of misalignment tolerance for inductive power transfer. IEEE Access 2020;8:191309–18. http://dx.doi.org/10.1109/ACCESS.2020. 3032563.

[4] Sagar A, Kashyap A, Nasab MA, Padmanaban S, Bertoluzzo M, Kumar A, Blaabjerg F. A comprehensive review of the recent development of wireless power transfer technologies for electric vehicle charging systems. IEEE Access 2023;11:83703–51. http://dx.doi.org/10.1109/ACCESS.2023.3300475.

[5] Kabbara W, Bensetti M, Phulpin T, Caillierez A, Loudot S, Sadarnac D. A control strategy to avoid drop and inrush currents during transient phases in a multi-transmitters DIPT system. Energies 2022;15(8). http://dx.doi.org/10.3390/ en15082911.

[6] Villa JL, Sallan J, Sanz Osorio JF, Llombart A. High-misalignment tolerant compensation topology for ICPT systems. IEEE Trans Ind Electron 2012;59(2):945–51. http://dx.doi.org/10.1109/TIE.2011.2161055.

[7] Aydin E, Aydemir MT, Aksoz A, El Baghdadi M, Hegazy O. Inductive power transfer for electric vehicle charging applications: A comprehensive review. Energies 2022;15(14). http://dx.doi.org/10.3390/en15144962.

[8] Chen Y, Zhang H, Park S-J, Kim D-H. A comparative study of S-S and LCCL-S compensation topologies in inductive power transfer systems for electric vehicles. Energies 2019;12(10). http://dx.doi.org/10.3390/en12101913.

[9] Feng H, Cai T, Duan S, Zhao J, Zhang X, Chen C. An LCC-compensated resonant converter optimized for robust reaction to large coupling variation in dynamic wireless power transfer. IEEE Trans Ind Electron 2016;63(10):6591–601. http: //dx.doi.org/10.1109/TIE.2016.2589922.

[10] Ramezani A, Farhangi S, Iman-Eini H, Farhangi B, Rahimi R, Moradi GR. Optimized LCC-series compensated resonant network for stationary wireless EV chargers. IEEE Trans Ind Electron 2019;66(4):2756–65. http://dx.doi.org/10. 1109/TIE.2018.2840502.

[11] Shen D, Du G, Zeng W, Yang Z, Li J. Research on optimization of compensation topology parameters for a wireless power transmission system with wide coupling coefficient fluctuation. IEEE Access 2020;8:59648–58. http://dx.doi.org/10. 1109/ACCESS.2020.2983612.

[12] She Z, Chen S, Chen Y, Zhang Y, Li H, Tang Y. Efficiency analysis of LCC-S and S-S inductive power transfer considering switching device and component losses. In: 2020 IEEE 9th international power electronics and motion control conference (IPEMC2020-ECCE Asia). 2020, p. 2956–60. http://dx.doi.org/10.1109/IPEMC-ECCEAsia48364.2020.9368208.

[13] Wireless power transfer for light-duty plug-in/electric vehicles and alignment methodology. 2020.

[14] García-Izquierdo O, Sanz J, Villa J, Martin-Segura G. Optimal design of a low-cost SAE JA2954 compliant WPT system using NSGA-II. Comput Ind Eng 2023;184:109536. http://dx.doi.org/10.1016/j.cie.2023.109536.

[15] Mai R, Yang B, Chen Y, Yang N, He Z, Gao S. A misalignment tolerant IPT system with intermediate coils for constant-current output. IEEE Trans Power Electron 2019;34(8):7151–5. http://dx.doi.org/10.1109/TPEL.2019.2898686.

[16] Chen Y, Mai R, Zhang Y, Li M, He Z. Improving misalignment tolerance for IPT system using a third-coil. IEEE Trans Power Electron 2019;34(4):3009–13. http://dx.doi.org/10.1109/TPEL.2018.2867919.

[17] Yan X-Y, Yang S-C, He H, Tang T-Q. An optimization model for wireless power transfer system based on circuit simulation. Phys A 2018;509:873–80. http://dx.doi.org/10.1016/j.physa.2018.06.058.

[18] Bosshard R, Kolar JW. Multi-objective optimization of 50 kW/85 kHz IPT system for public transport. IEEE J Emerg Sel Top Power Electron 2016;4(4):1370–82. http://dx.doi.org/10.1109/JESTPE.2016.2598755.

[19] Tan L, Tang Z, Zhong R, Huang X, Liu H, Chen C. An optimization strategy based on dimension reduction method in wireless charging system design. IEEE Access 2019;7:151733–45. http://dx.doi.org/10.1109/ACCESS.2019.2948196.

[20] Luo Z, Wei X, Covic GA. Multi-objective optimization of double D coils for wireless charging system. In: 2018 IEEE international power electronics and application conference and exposition. PEAC, 2018, p. 1–6. http://dx.doi.org/10.1109/PEAC.2018.8589975.

[21] Bertoluzzo M, Di Barba P, Forzan M, Mognaschi ME, Sieni E. Optimization of compensation network for a wireless power transfer system in dynamic conditions: A circuit analysis approach. Algorithms 2022;15(8). http://dx.doi.org/10.3390/a15080261.

[22] Pei Y, Pichon L, Le Bihan Y, Bensetti M, Dessante P. Fast shielding optimization of an inductive power transfer system for electric vehicles. IEEE Access 2022;10:91227–34. http://dx.doi.org/10.1109/ACCESS.2022.3198953.

[23] Yilmaz T, Hasan N, Zane R, Pantic Z. Multi-objective optimization of circular magnetic couplers for wireless power transfer applications. IEEE Trans Magn 2017;53(8):1–12. http://dx.doi.org/10.1109/TMAG.2017.2692218.

[24] Hasan N, Yilmaz T, Zane R, Pantic Z. Multi-objective particle swarm optimization applied to the design of wireless power transfer systems. In: 2015 IEEE wireless power transfer conference. WPTC, 2015, p. 1–4. http://dx.doi.org/10.1109/WPT.2015.7139138.

[25] Yao Y, Wang Y, Liu X, Pei Y, Xu D, Liu X. Particle swarm optimization-based parameter design method for s/CLC-compensated IPT systems featuring high tolerance to misalignment and load variation. IEEE Trans Power Electron 2019;34(6):5268–82. http://dx.doi.org/10.1109/TPEL.2018.2870530.

[26] Yang J, Liu R, Tong Q, Yang X, Liu Q, Yao A. Multi-objective optimization of LCC-S-compensated IPT system for improving misalignment tolerance. Appl Sci 2023;13(6). http://dx.doi.org/10.3390/app13063666.

[27] Talbi E-G. Metaheuristics - From design to implementation. Wiley; 2009.

[28] Talbi E-G. A unified taxonomy of hybrid metaheuristics with mathematical programming, constraint programming and machine learning. In: Talbi E-G, editor. Hybrid metaheuristics. Berlin, Heidelberg: Springer Berlin Heidelberg; 2013, p. 3–76. http://dx.doi.org/10.1007/978-3-642-30671-6_1.

[29] Talbi E-G. A taxonomy of hybrid metaheuristics. J Heuristics 2002;8:541–64.

[30] Otomo Y, Igarashi H. A 3-D topology optimization of magnetic cores for wireless power transfer device. IEEE Trans Magn 2019;55(6):1–5. http://dx.doi.org/10.1109/TMAG.2019.2900744.

[31] Sato T, Watanabe K, Igarashi H. Multimaterial topology optimization of electric machines based on normalized Gaussian network. IEEE Trans Magn 2015;51(3):1–4. http://dx.doi.org/10.1109/TMAG.2014.2359972.

[32] Wolpert D, Macready W. No free lunch theorems for optimization. IEEE Trans Evol Comput 1997;1(1):67–82. http://dx.doi.org/10.1109/4235.585893.

[33] Liu X, Clare L, Yuan X, Wang C, Liu J. A design method for making an LCC compensation two-coil wireless power transfer system more energy efficient than an SS counterpart. Energies 2017;10(9). http://dx.doi.org/10.3390/en10091346.

[34] Cirimele V, Torchio R, Villa JL, Freschi F, Alotto P, Codecasa L, di Rienzo L. Uncertainty quantification for SAE J2954 compliant static wireless charge components. IEEE Access 2020;8:171489–501.

[35] Aebischer HA. Inductance formula for rectangular planar spiral inductors with rectangular conductor cross section. Adv Electromagn 2020;9(1):1–18. http://dx.doi.org/10.7716/aem.v9i1.1346.

[36] Acero J, Lope I, Carretero C, Burdío J. Analysis of winding loss and optimization of inductive power transfer coils. In: 2020 IEEE 29th international symposium on industrial electronics. ISIE, 2020, p. 1435–41. http://dx.doi.org/10.1109/ISIE45063.2020.9152283.

[37] García O, Sanz JF, Villa JL, Alonso MA, Perie JM, Acerete R. Modelling of a high-misalignment tolerant WPT system for dynamic charge with a long secondary pad. In: 2020 IEEE international symposium on circuits and systems. ISCAS, 2020, p. 1–5. http://dx.doi.org/10.1109/ISCAS45731.2020.9181206.

[38] Li J, Tan L, Huang X, Wang R, Zhang M. The influence of substrate size changes on the coil resistance of the wireless power transfer system. Electronics 2020;9(6). http://dx.doi.org/10.3390/electronics9061025.

[39] Tourkhani F, Viarouge P. Accurate analytical model of winding losses in round Litz wire windings. IEEE Trans Magn 2001;37(1):538–43. http://dx.doi.org/10.1109/20.914375.

[40] Woodworth A, Sixel WA, Edwards R, Jansen R, McCormick S, Robbie M, Smith A, Naghipour P, Shin EE. Thermal analysis of potted litz wire for high power density aerospace electric machines. In: AIAA propulsion and energy 2019 forum. http://dx.doi.org/10.2514/6.2019-4509.

[41] Paul AK. Current density characterization of litz wires used in induction heating coils: A practical approach. In: 2018 IEEE international conference on power electronics, drives and energy systems. PEDES, 2018, p. 1–6. http://dx.doi.org/10.1109/PEDES.2018.8707901.

[42] Beyer H-G, Deb K. On self-adaptive features in real-parameter evolutionary algorithms. IEEE Trans Evol Comput 2001;5:250–70.

[43] Deb K, Agrawal RB. Simulated binary crossover for continuous search space. Complex Systems 1995;9.

[44] Raghuwanshi MM, Kakde OG, Gandhi R. Survey on multiobjective evolutionary and real coded genetic algorithms. 2004.

[45] Chacón J, Segura C. Analysis and enhancement of simulated binary crossover. In: 2018 IEEE congress on evolutionary computation. CEC, 2018, p. 1–8. http://dx.doi.org/10.1109/CEC.2018.8477746.

[46] Deb K, Kumar A. Real-coded genetic algorithms with simulated binary crossover: Studies on multimodal and multiobjective problems. Complex Systems 1995;9.

[47] Jung D, Choi YH, Kim JH. Multiobjective automatic parameter calibration of a hydrological model. Water 2017;9(3). http://dx.doi.org/10.3390/w9030187, URL https://www.mdpi.com/2073-4441/9/3/187.

[48] Zhang R, Moreira M, Corte-Real J. Multi-objective calibration of the physically based, spatially distributed SHETRAN hydrological model. J Hydroinform 2015;18(3):428–45. http://dx.doi.org/10.2166/hydro.2015.219, arXiv:https://iwaponline.com/jh/article-pdf/18/3/428/478800/jh0180428.pdf.

[49] Sinha A. Bilevel multi-objective optimization problem solving using progressively interactive EMO. In: Takahashi RHC, Deb K, Wanner EF, Greco S, editors. Evolutionary multi-criterion optimization. Berlin, Heidelberg: Springer Berlin Heidelberg; 2011, p. 269–84.

[50] Deb K, Pratap A, Agarwal S, Meyarivan T. A fast and elitist multiobjective genetic algorithm: NSGA-II. IEEE Trans Evol Comput 2002;6(2):182–97. http://dx.doi.org/10.1109/4235.996017.

[51] Sinha A. Progressively interactive evolutionary multiobjective optimization (Doctoral thesis), School of Business; 2011, p. vi, 129 s., URL http://urn.fi/URN:ISBN:978-952-60-4052-3.

[52] Pétrowski A, Ben Hamida S. Multi-objective optimization. 2017, p. 165–82. http://dx.doi.org/10.1002/9781119136378.ch5.

[53] Tan K, Lee T, Khor E. Evolutionary algorithms for multi-objective optimization: performance assessments and comparisons. In: Proceedings of the 2001 congress on evolutionary computation (IEEE cat. no.01TH8546). Vol. 2, 2001, p. 979–86. http://dx.doi.org/10.1109/CEC.2001.934296, vol. 2.

[54] Zitzler E, Brockhoff D, Thiele L. The hypervolume indicator revisited: On the design of Pareto-compliant indicators via weighted integration. In: Obayashi S, Deb K, Poloni C, Hiroyasu T, Murata T, editors. Evolutionary multi-criterion optimization. Berlin, Heidelberg: Springer Berlin Heidelberg; 2007, p. 862–76.

[55] Zitzler E, Deb K, Thiele L. Comparison of multiobjective evolutionary algorithms: Empirical results. Evol Comput 2000;8(2):173–95. http://dx.doi.org/10.1162/106365600568202.

[56] Icnirp guidelines. 2010.

[57] FERROXCUBE. Material 3c90. 2002.

[58] Chang R, Quan L, Zhu X, Zong Z, Zhou H. Design of a wireless power transfer system for EV application based on finite element analysis and MATLAB simulation. In: 2014 IEEE conference and expo transportation electrification Asia-Pacific (ITEC Asia-Pacific). 2014, p. 1–4. http://dx.doi.org/10.1109/ITEC-AP.2014.6941225.

[59] Zhu C, Liu K, Yu C, Ma R, Cheng H. Simulation and experimental analysis on wireless energy transfer based on magnetic resonances. In: 2008 IEEE vehicle power and propulsion conference. 2008, p. 1–4. http://dx.doi.org/10.1109/VPPC.2008.4677400.